Supporting Information

Ultramicroporous hydrogen-bond decorated robust metal-organic framework for high xenon capture performances

Minjung Kang,† Jong Hyeak Choe,† Hyojin Kim,† Hongryeol Yun,† Dae Won Kim† and Chang Seop Hong†,*

†Department of Chemistry, Korea University

Seoul 02841, Republic of Korea

E-mail: cshong@korea.ac.kr

S1. Experimental section

Gram-scale synthesis of Ni(AIN)$_2$. **Ni(AIN)$_2$** can also be prepared in gram-scale. $Ni(OAc)_2 \cdot 4H_2O$ (2.49 g, 10 mmol), HAIN (2.76 g, 20 mmol), DMF (90 mL) and ACN (60 mL) were loaded in a 250 mL round bottom flask and stirred at room temperature for about 1 h. After stirring the mixture, trimethylamine (1.125 mL) was added to it and stirred for another 1 h. The mixture was reacted under reflux at 150 ^{o}C for 5 days with sitrring. Green powder of **Ni(AIN)$_2$** were collected by filtration and washed with fresh DMF for 12 h at 80 ^{o}C to remove residual ligands. The final product was isolated by filtration, washed with methanol, and dried under vacuum. Yield: 3.84 g (92.4%) The PXRD and gas uptakes matched well with the milligram-scale sample. (Fig. S14-15)

Single-crystal X-ray crystallography. X-ray data for single crystals of **Ni(AIN)$_2$** was recorded with a cryoloop mounted on a goniometer head in a cold stream of liquid nitrogen. The diffraction data were measured with synchrotron radiation using a Rayonix MX225HS CCD area detector with a silicon (111) double-crystal monochromator at the Pohang Accelerator Laboratory, Korea. The PAL BL2D-SMDC program[1] was used for data collection and HKL3000sm[1, 2] was used for cell refinement, reduction, and absorption correction. The structure was solved by direct methods and refined by full-matrix least-squares analysis using anisotropic thermal parameters for non-hydrogen atoms with the SHELXTL program. All hydrogen atoms were calculated at idealized positions and refined with the riding models. To account for this electron density, the program SQUEEZE, a part of the PLATON[3] package of crystallographic software, was used to calculate the solvent disorder area and remove its contribution to the overall intensity data. CCDC 2192392 (**Ni(AIN)$_2$**) contains the supplementary crystallographic data for this paper.

Breakthrough experiments. The breakthrough curves of mixed gas Xe/Kr (2:8, v/v) for **Ni(AIN)$_2$** were performed by a BELCAT-II linked with BELMASS mass spectrometer. A fixed-bed column filled with the pelletized samples (425 – 600 μm) was prepared and the total gas flow rate was fixed to total 20 sccm. The flow rates of binary mixture Xe/Kr were controlled at 4 sccm for 1:1, and 1 sccm for 1:15, respectively, balanced with He gas. Before breakthrough measurements, all samples were activated at 160 ^{o}C for 12 h. All outgas were continuously monitored by the mass spectrometer. The adsorbed amount of each gas was calculated with the ChemMaster program.[4] In case of the cyclic test, the samples were regenerated at 25 ^{o}C for 2 h before each cycle.

Computational methods. Grand canonical Monte Carlo (GCMC) simulations were performed for the gas adsorption in the framework and the binding energy calculation by the Sorption module of Material Studio (Accelrys. Materials Studio Getting Started, release 2019).[5] The framework was considered to be rigid, and the Xe and Kr molecules were used. The partial charges for atoms of the framework were derived from QEq method and QEq_charged1.1 parameter. 2x2x2 unit cells were used during the simulations. The sorption geometries were optimized by Smart algorithm with ultra-fine quality. All parameters for the atoms were modeled with the universal force field (UFF) embedded in the MS modeling package. A cutoff distance of 18.5 Å was used for electrostatic interactions, and the simulation method of the interactions were calculated by using Ewald & Group summation. For each run, the 2×10^5 maximum loading steps, 2×10^7 production steps were employed.

Isosteric heat of adsorption calculations. The coverage-dependent adsorption enthalpy profiles were calculated from the sorption data measured at 273, 298, and 323 K by virial fitting method and Clausius-Claperyron equation. A virial-type expression was used (eq. S1), which is composed of parameters a_i and b_i, which are independent of temperature. In eq. S1, P is the pressure in atm, N is the adsorbed amount in mmol g^{-1}, T is the temperature in Kelvin, a_i and b_i are the virial coefficients, and m and n represent the number of coefficients required to adequately describe the isotherms.

$$ln\, p = \ln N + \frac{1}{T}\sum_{i=0}^{l} a_i n^i + \sum_{j=0}^{m} b_j n^j \qquad \text{(eq. S1)}$$

To calculate Q_{st}, the fitting parameters from the Eq. S1 were used for the Eq. S2.

$$Q_{st} = -R\left[\frac{\partial ln ln\, p}{\partial\left(\frac{1}{T}\right)}\right]_n = -R\sum_{i=0}^{l} a_i n^i \qquad \text{(eq. S2)}$$

S2. Structure and analytical characterizations

Table S1 Crystal data and structure refinement for **$Ni(AIN)_2$**.

Identification code	**$Ni(AIN)_2$**
Empirical formula	C12 H10 N4 Ni1 O4
Formula weight	332.93
Temperature	293(2) K
Wavelength	0.700 Å
Crystal system	Orthorhombic
Space group	Pnn2
Unit cell dimensions	a = 11.985(2) Å α= 90°
	b = 6.8910(14) Å β= 90°
	c = 10.624(2) Å γ = 90°
Volume	877.4(3) $Å^3$
Z	2
Density (calculated)	1.260 Mg/m^3
Absorption coefficient	1.073 mm^{-1}
F(000)	340
Crystal size	0.039 x 0.037 x 0.035 mm^3
Theta range for data collection	2.523 to 33.280°.
Index ranges	-17<=h<=17, -9<=k<=10, -15<=l<=15
Reflections collected	9439
Independent reflections	2963 [R(int) = 0.0792]
Completeness to theta = 24.835°	100 %
Refinement method	Full-matrix least-squares on F^2
Data / restraints / parameters	2963 / 1 / 97
Goodness-of-fit on F^2	0.781
Final R indices [I>2sigma(I)]	R1 = 0.0655, wR2 = 0.1929
R indices (all data)	R1 = 0.0964, wR2 = 0.2289
Absolute structure parameter	0.279(10)
Extinction coefficient	0.038(13)
Largest diff. peak and hole	0.934 and -1.457 e.$Å^{-3}$

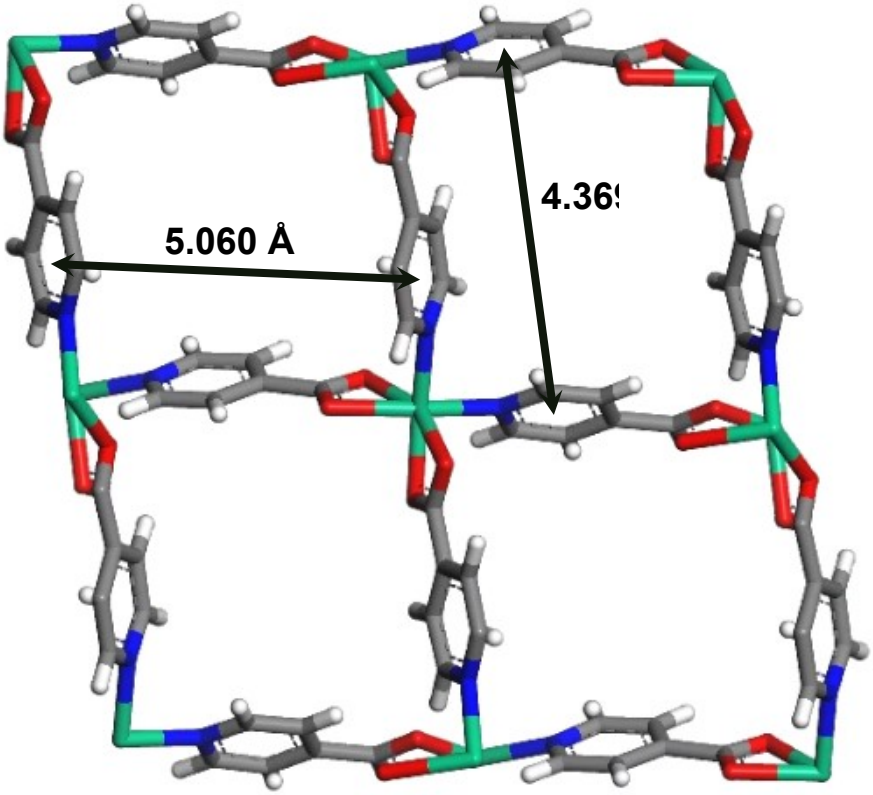

Fig. S1 Single crystal structure of **Ni(IN)$_2$** with rectangular 1D pores.

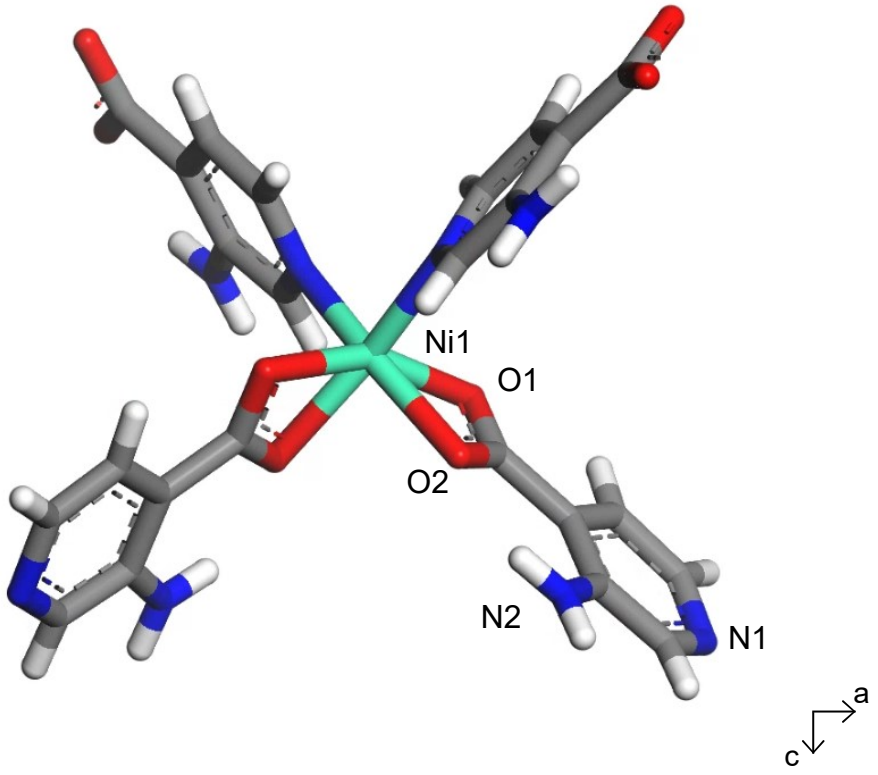

Fig. S2 Coordination environment of Ni^{2+} ion in the **Ni(AIN)$_2$** structure.

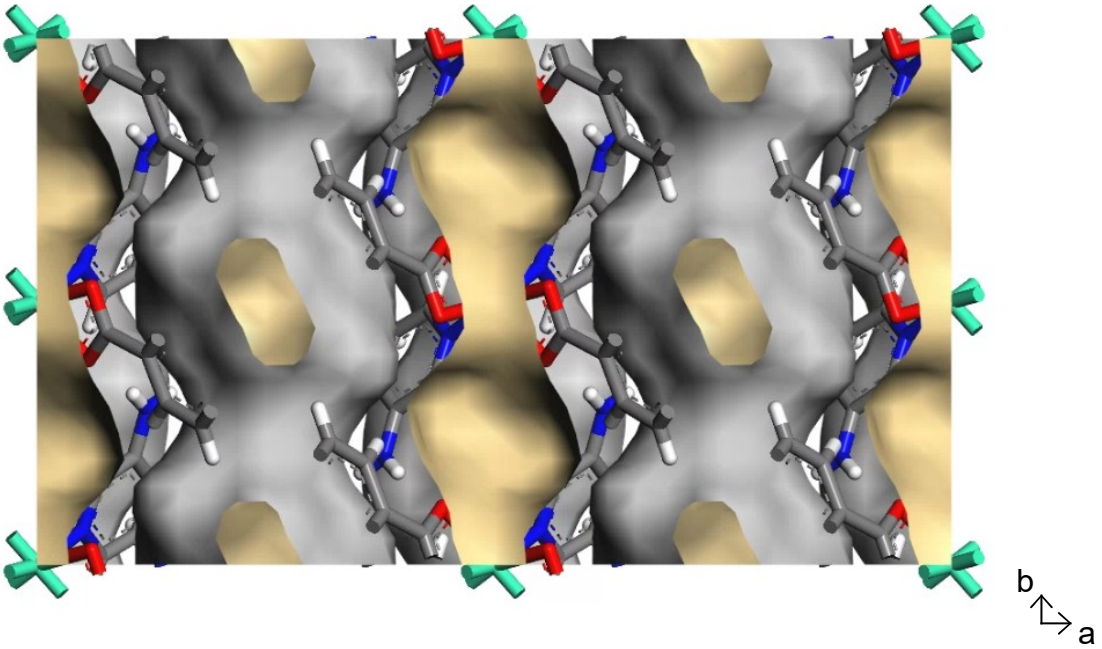

Fig. S3 Connolly surface representation of **Ni(AIN)$_2$** along the c-axis direction. (probe diameter = 1.0 Å).

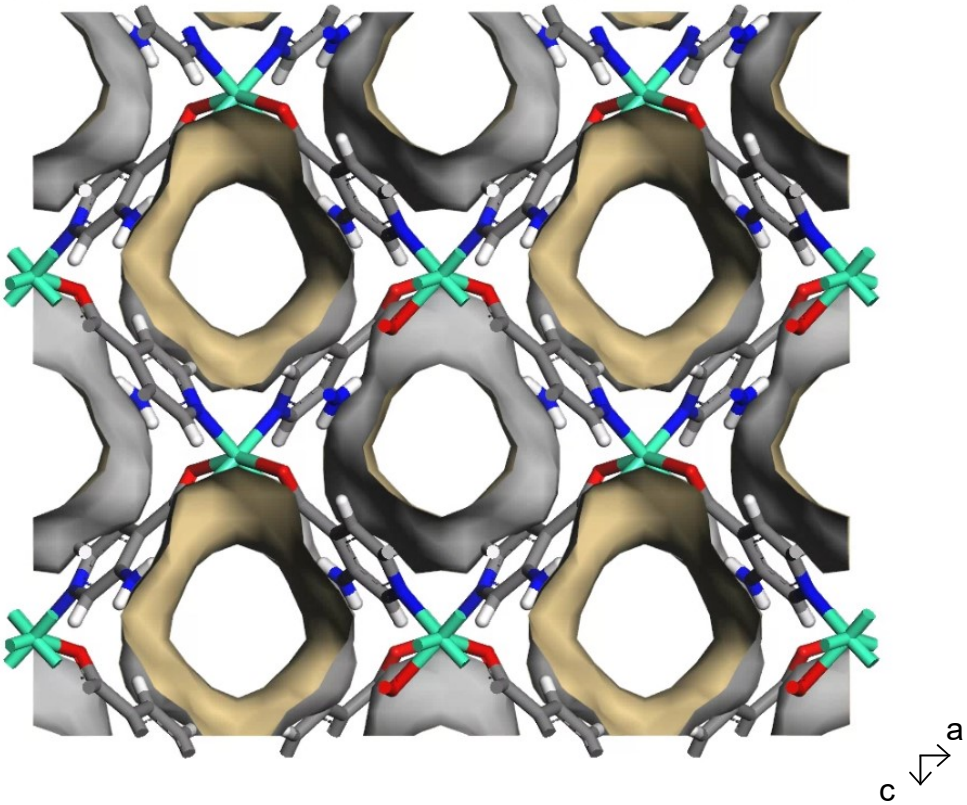

Fig. S4 Connolly surface representation of **Ni(AIN)$_2$** along the b-axis direction (probe diameter = 1.0 Å).

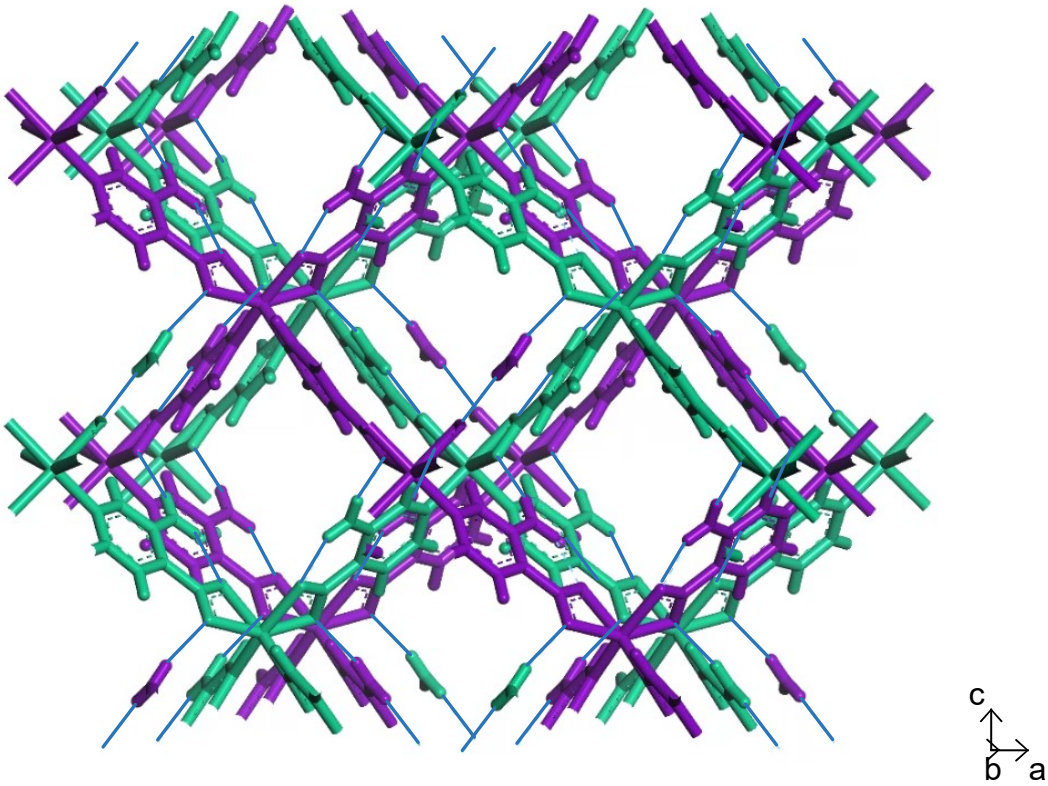

Fig. S5 Two-fold interpenetrated structure of **Ni(AIN)$_2$**. The sky-blue dotted lines denote intra- and inter-net hydrogen bonds.

(a)

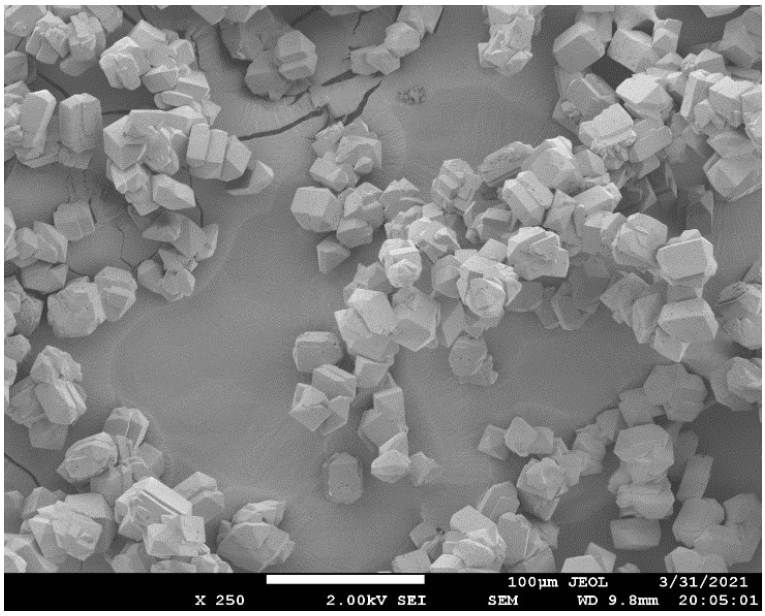

(b)

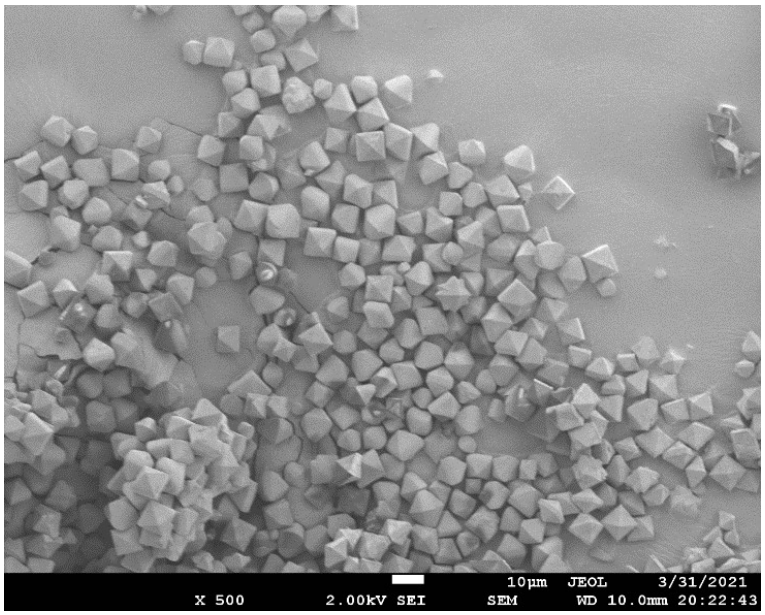

Fig. S6 SEM images of (a) **Ni(IN)$_2$** and (b) **Ni(AIN)$_2$**.

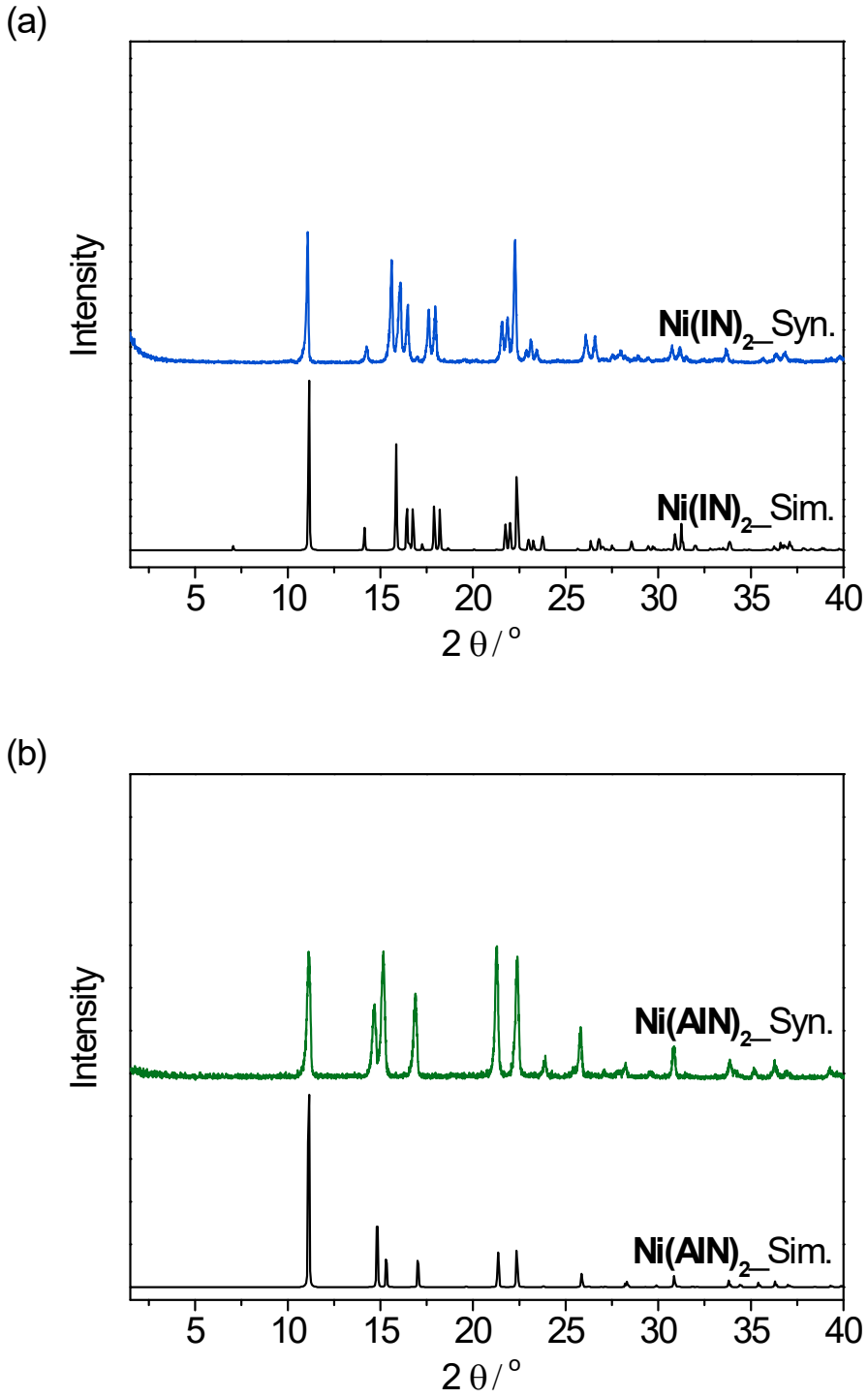

Fig. S7 PXRD patterns of (a) **Ni(IN)$_2$** and (b)**Ni(AIN)$_2$**, together with the similated patterns.

Table S2 Elemental analysis data.

Compounds		C (%)	N (%)	H (%)
[**Ni(IN)$_2$**]·DMF0.5H_2O *(As made)*	Exp.	46.60	10.84	4.11
	Calc.	46.80	10.91	4.19
	Error	0.20	0.07	0.08
[**Ni(AIN)$_2$**]·DMF0.5H_2O *(As made)*	Exp.	43.20	16.91	4.20
	Calc.	43.41	16.87	4.37
	Error	0.21	0.04	0.17
[**Ni(IN)$_2$**]·0.5H_2O *(Activated)*	Exp.	46.11	8.60	2.76
	Calc.	46.21	8.98	2.91
	Error	0.10	0.38	0.15
[**Ni(AIN)$_2$**]·0.8H_2O *(Activated)*	Exp.	41.53	16.07	3.11
	Calc.	41.50	16.13	3.37
	Error	0.03	0.06	0.26

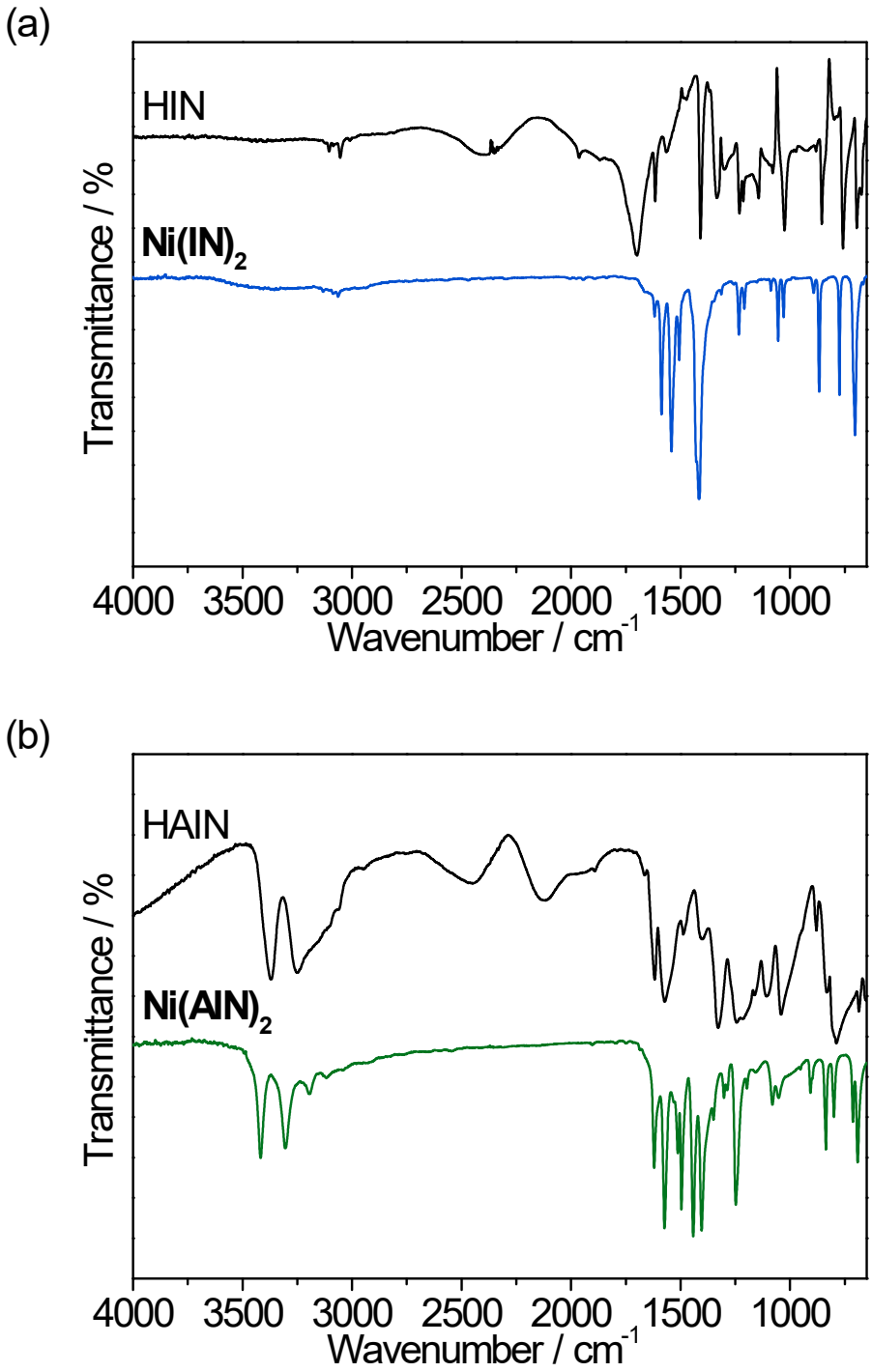

Fig. S8 IR spectra of (a) **Ni(IN)$_2$** and HIN, and (b) **Ni(AIN)$_2$** and HAIN.

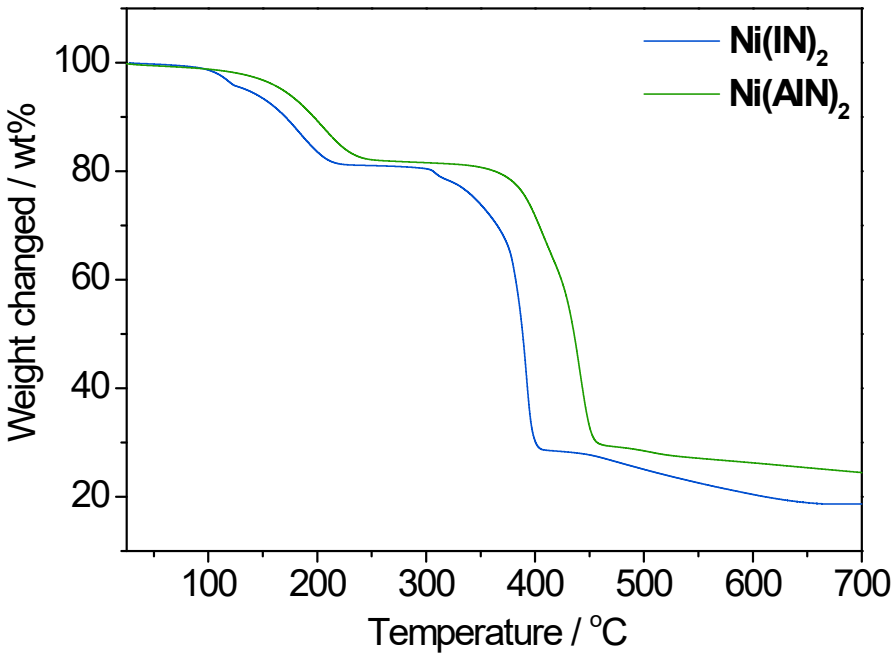

Fig. S9 TGA curves of **Ni(IN)$_2$** and **Ni(AIN)$_2$**.

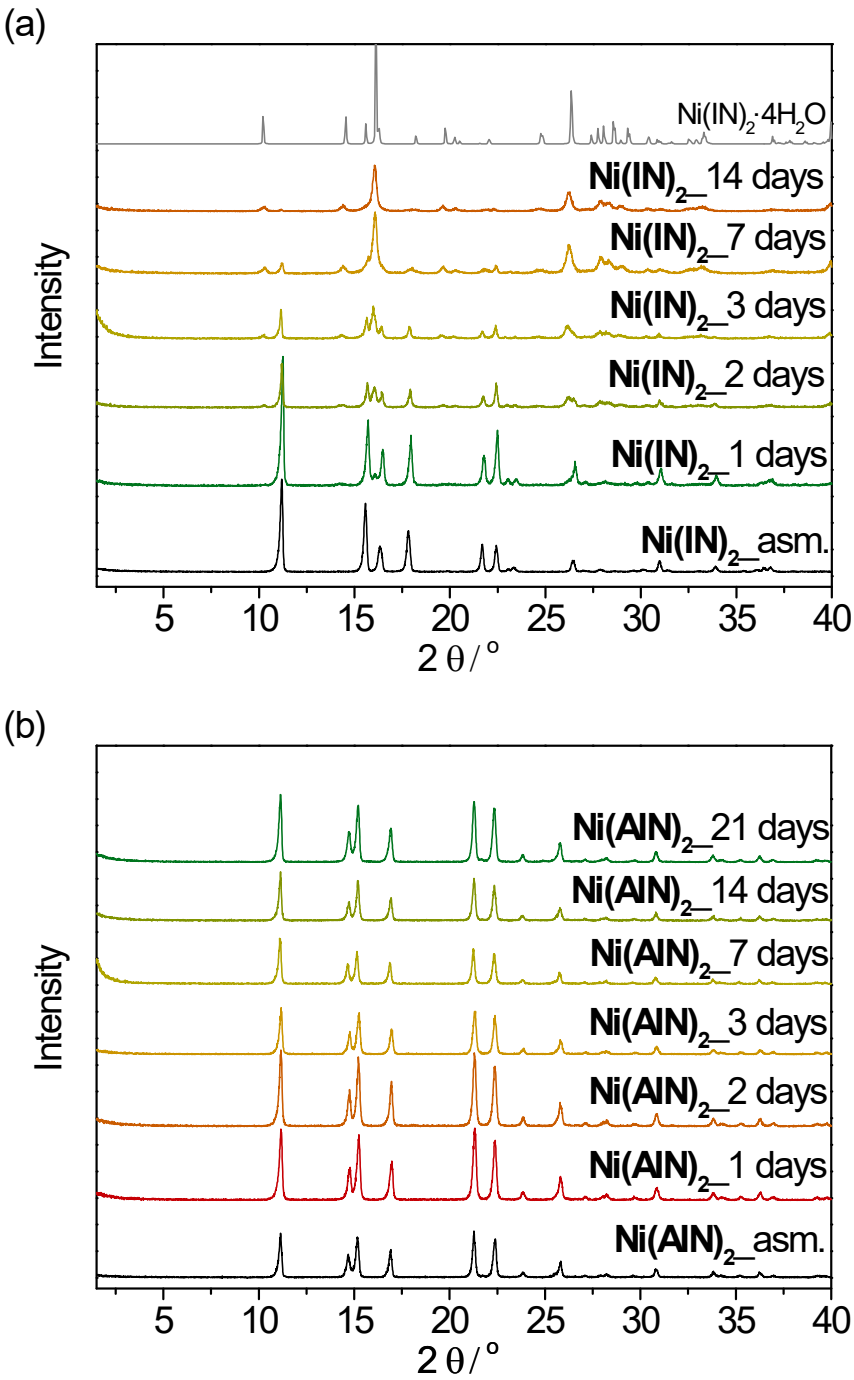

Fig. S10 PXRD pattern after exposure to 40% relative humidity up to (a) 14 days for **Ni(IN)$_2$** and (b) 21 days for **Ni(AIN)$_2$**.

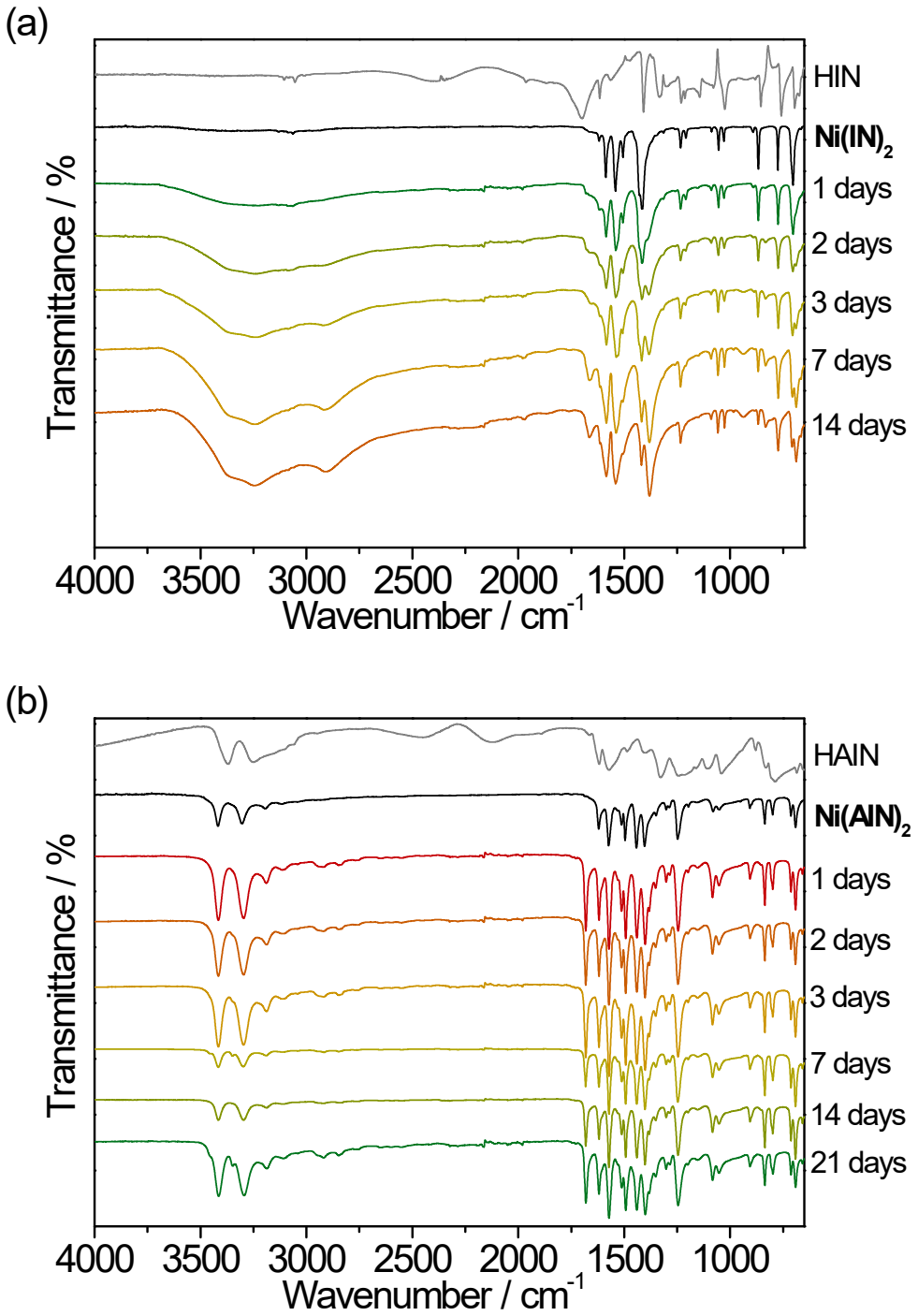

Fig. S11 IR spactra after exposure to 40% relative humidity up to (a) 14 days for **Ni(IN)$_2$** and (b) 21 days for **Ni(AIN)$_2$** .

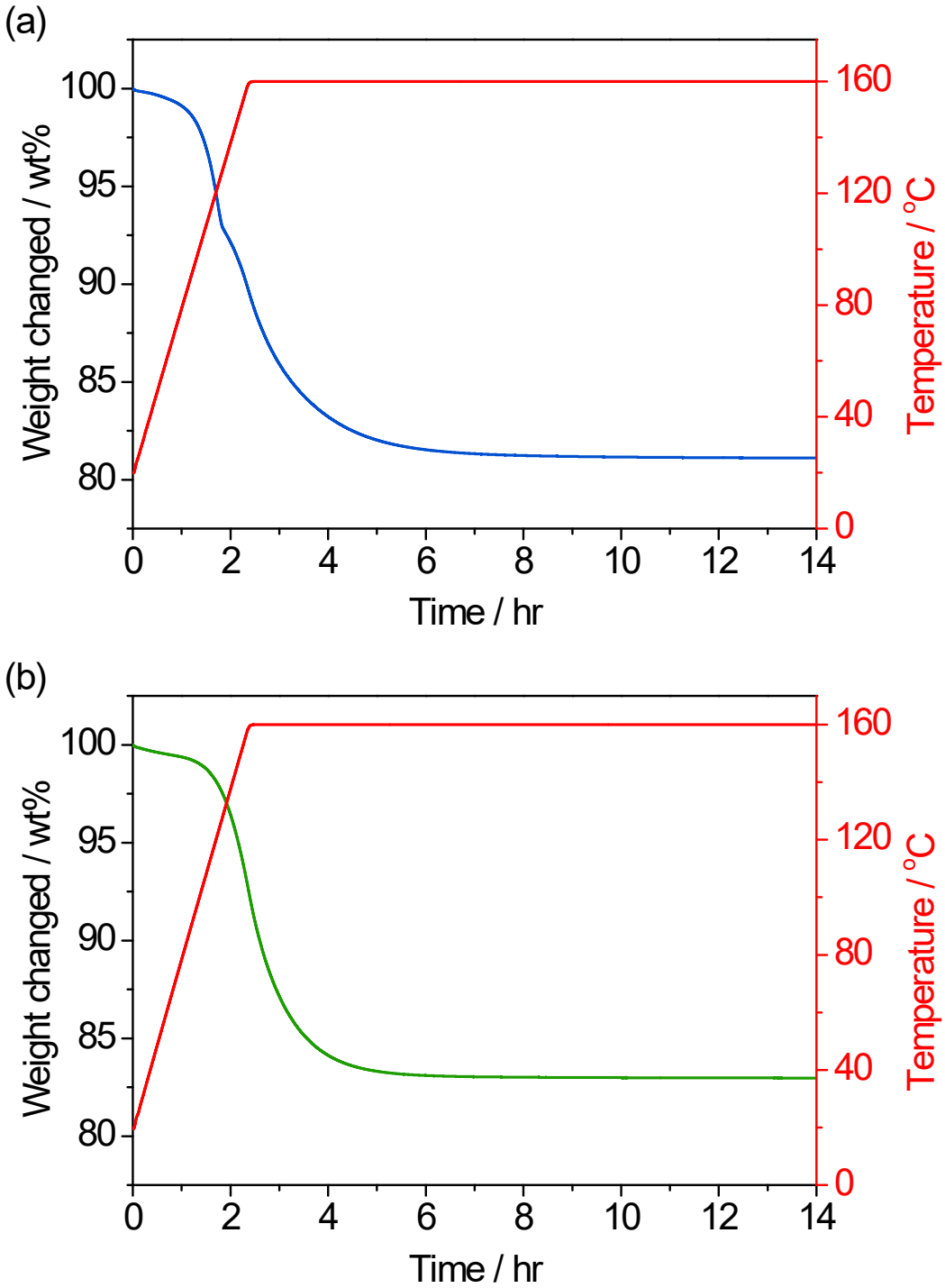

Fig. S12 TGA curves of (a) **Ni(IN)$_2$** and (b) **Ni(AIN)$_2$** under isothermal conditions for 12 h at 160 °C, an activation condition before gas sorption measurements.

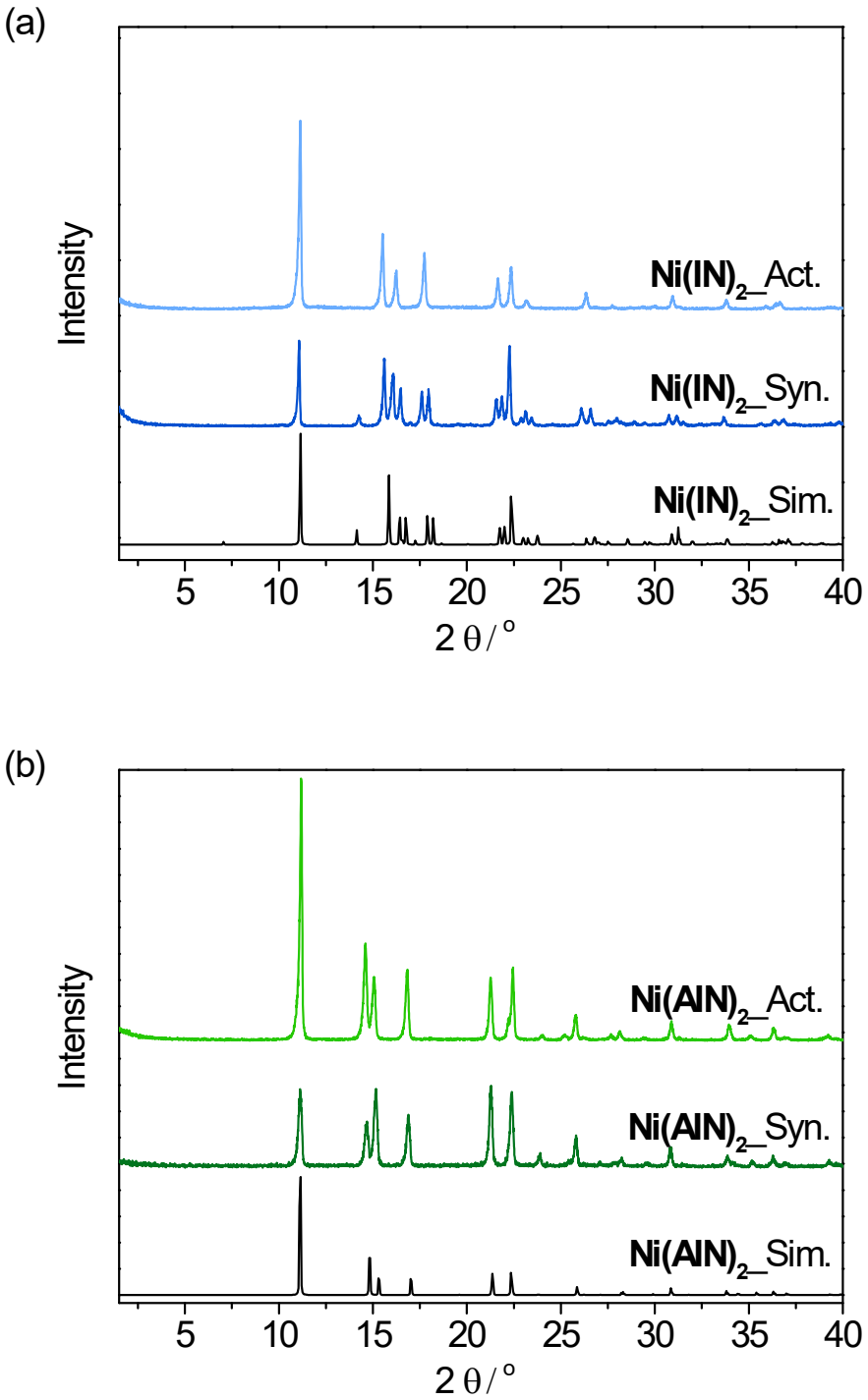

Fig. S13 PXRD patterns of (a) activated **Ni(IN)$_2$** and (b) **Ni(AIN)$_2$**. Each structure retained its crystallinity after activation.

S3. Adsorption studies

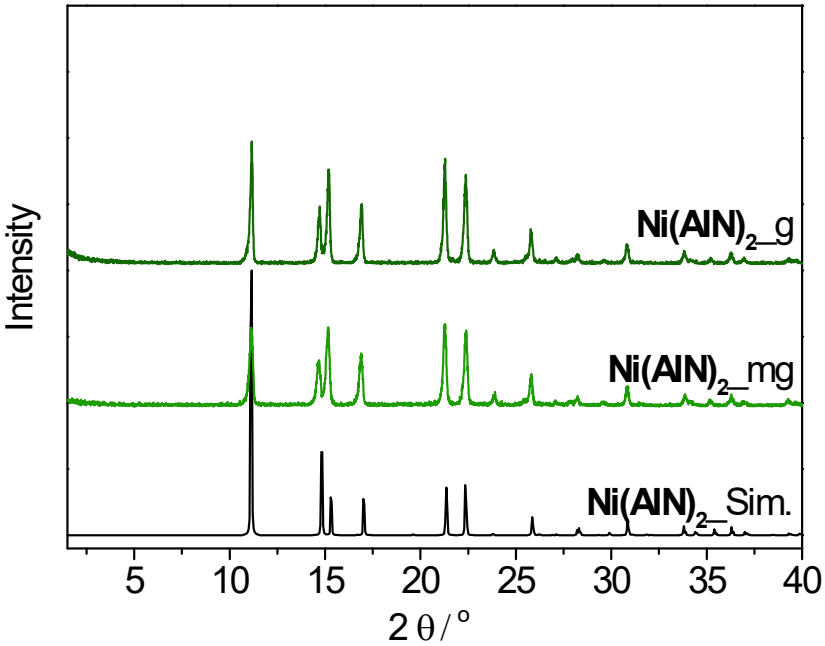

Fig. S14 PXRD profiles of samples prepared in gram scale and milligram scale.

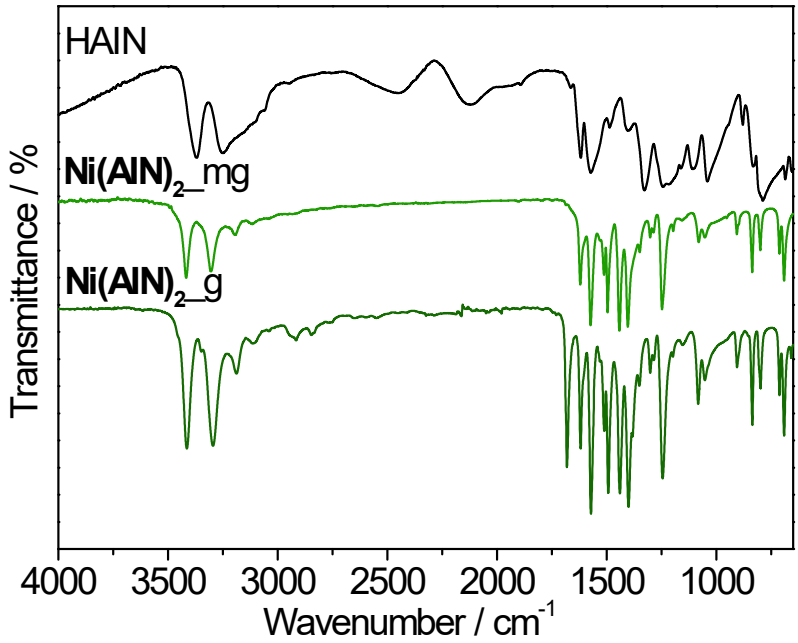

Fig. S15 IR spectra of samples prepared in gram scale and milligram scale.

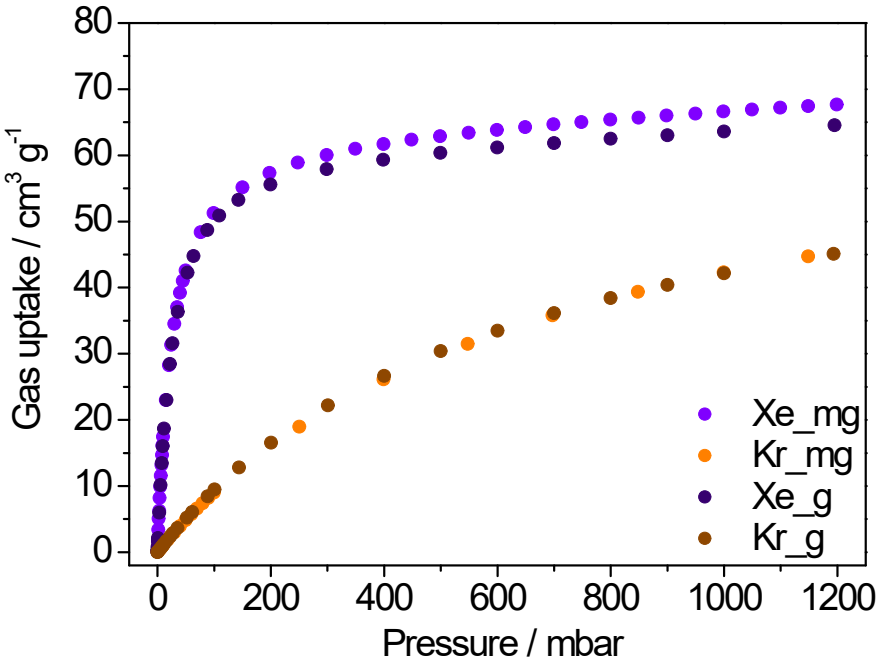

Fig. S16 Single component Xe and Kr isotherms of samples at room temperature, prepared in gram scale and milligram scale.

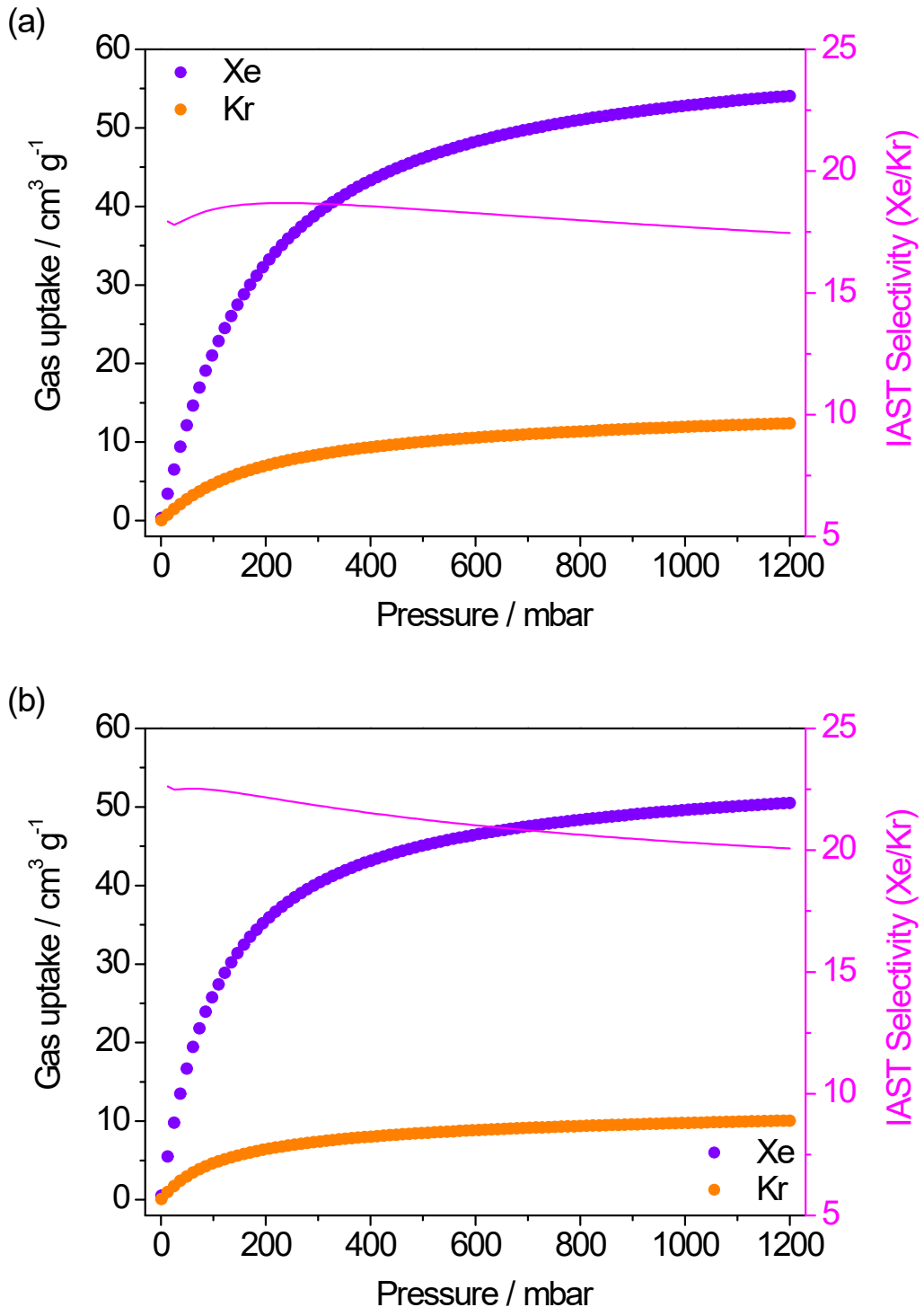

Fig. S17 IAST model-predicted adsorption isotherms and selectivity of (a) **Ni(IN)$_2$** and (b) **Ni(AIN)$_2$**.

Table S3 Fitting parameters for **Ni(IN)$_2$** to the dual-site Langmuir-Freundlich isothem model at different gases and temperatures.

MOF	**Ni(IN)$_2$**					
Gas	Xe			Kr		
Temp.	273 K	298 K	323 K	273 K	298 K	323 K
q_1	187.212	48.127	3.05757	34.529	24.8458	4.3652
k_1	3.15547E-06	2.34716E-05	1.04497E-06	0.000865838	0.000389489	0.000567696
n_1	0.44573	0.467237	0.313113	0.922744	0.83827	0.674891
q_2	62.4024	67.113	74.1648	56.7709	63.9373	81.1094
b_2	0.0819847	0.0256792	0.00841015	0.00271562	0.00111312	0.000481999
n_2	1.21461	1.15015	1.07036	1.05514	1.05711	1.05156
R^2	0.999977	0.999992	0.999988	0.999999	1	0.999999

*q_1, q_2: Maximum adsorption capacity (cm^3 g^{-1}); k_1, k_2: Equilibrium constant (kPa^{-1}); n_1, n_2: Constant related to the strength of adsorption.

Table S4 Fitting parameters for **Ni(AIN)$_2$** to the dual-site Langmuir-Freundlich isothem model at different gases and temperatures.

MOF	**Ni(AIN)$_2$**					
Gas	Xe			Kr		
Temp.	273 K	298 K	323 K	273 K	298 K	323 K
q_1	64.0072	78.2381	14.5598	34.6921	0.0115306	0.104247
k_1	0.129417	1.73732E-05	0.00205891	0.00493981	0.249992	0.0995717
n_1	1.04435	0.496304	0.734969	1.08227	4.05966	0.860332
q_2	30.4925	58.3616	55.2035	46.9308	72.1866	75.9922
b_2	0.000604347	0.0421174	0.0152965	0.00142424	0.00141474	0.000639294
n_2	1.15305	1.07506	1.06798	0.889621	0.995324	1.0037
R^2	0.999998	0.999998	0.999999	0.999997	0.999998	0.999996

*q_1, q_2: Maximum adsorption capacity (cm^3 g^{-1}); k_1, k_2: Equilibrium constant (kPa^{-1}); n_1, n_2: Constant related to the strength of adsorption.

Table S5 Fitting parameters to the dual-site Langmuir isothem model and Henry coefficient (H_b) at different gases and temperatures.

MOF	Gas	Temp. (K)	Adsorbed amount $q_{m,1}$ (mmol g^{-1})	Equilibrium constant b_1 (kPa^{-1})	Adsorbed amount $q_{m,2}$ (mmol g^{-1})	Equilibrium constant b_2 (kPa^{-1})	Correlation coefficient (R^2)	H_b (mmol g^{-1} kPa^{-1})
Ni(IN)$_2$	Xe	273	1.8541	0.605469	1.50196	0.605469	0.999335	2.03199
		298	1.22711	0.207485	2.18152	0.207485	0.999788	0.70724
		323	2.05062E-16	1.10681	3.45255	0.074566	0.999806	0.257444
	Kr	273	1.19775	0.020294	2.68528	0.020294	0.999994	0.078802
		298	3.86922E-11	0.001373	3.89974	0.009089	0.999993	0.035445
		323	4.05433	0.004292	0.418774	0.000228	0.999998	0.017497
Ni(AIN)$_2$	Xe	273	2.92485	1.20979	28.9325	0.000149	0.999975	3.542773
		298	452.112	3.43503E-06	2.88884	0.372041	0.999974	1.07632
		323	0.522254	0.127227	2.43146	0.127227	0.99998	0.375792
	Kr	273	3.02593	0.0352769	32.5988	5.22444E-05	0.999999	0.108449
		298	2.8833	0.0154938	0.611235	0.002861	1	0.046422
		323	0.002127	4.69792	3.38382	0.006418	0.999997	0.03171

Table S6 Summary of IAST selectivity and Henry's selectivity at different temperatures.

MOF		Temperature	Selectivity
$Ni(IN)_2$	IAST Selectivity	273 K	19.15
		298 K	17.70
		323 K	13.45
	Henry's Selectivity	273 K	25.79
		298 K	19.95
		323 K	14.71
$Ni(AIN)_2$	IAST Selectivity	273 K	24.39
		298 K	20.32
		323 K	15.32
	Henry's Selectivity	273 K	32.67
		298 K	23.19
		323 K	11.85

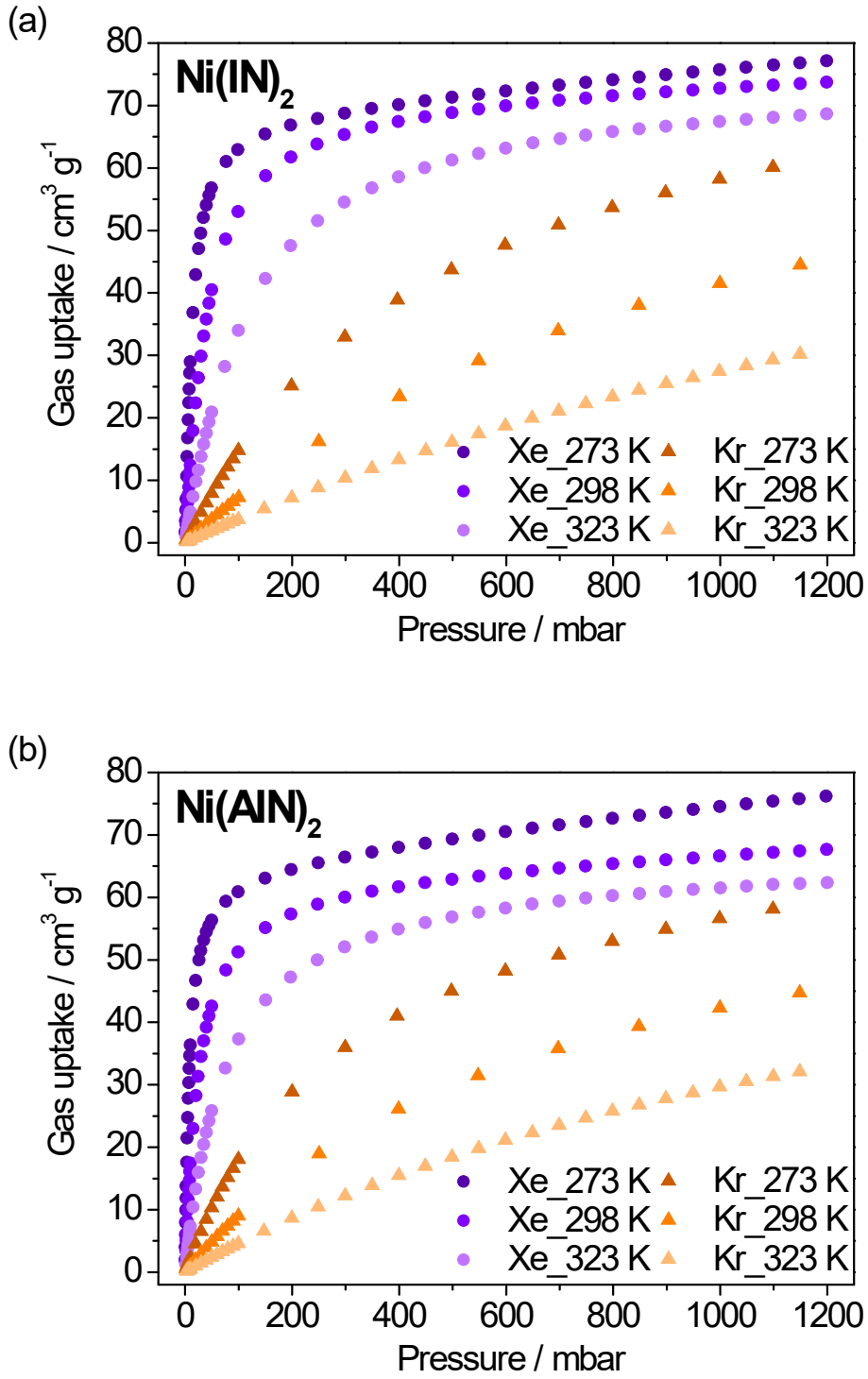

Fig. S18 Xe and Kr isotherms of (a) **Ni(IN)$_2$** and (b) **Ni(AIN)$_2$** at 273, 298, and 323 K.

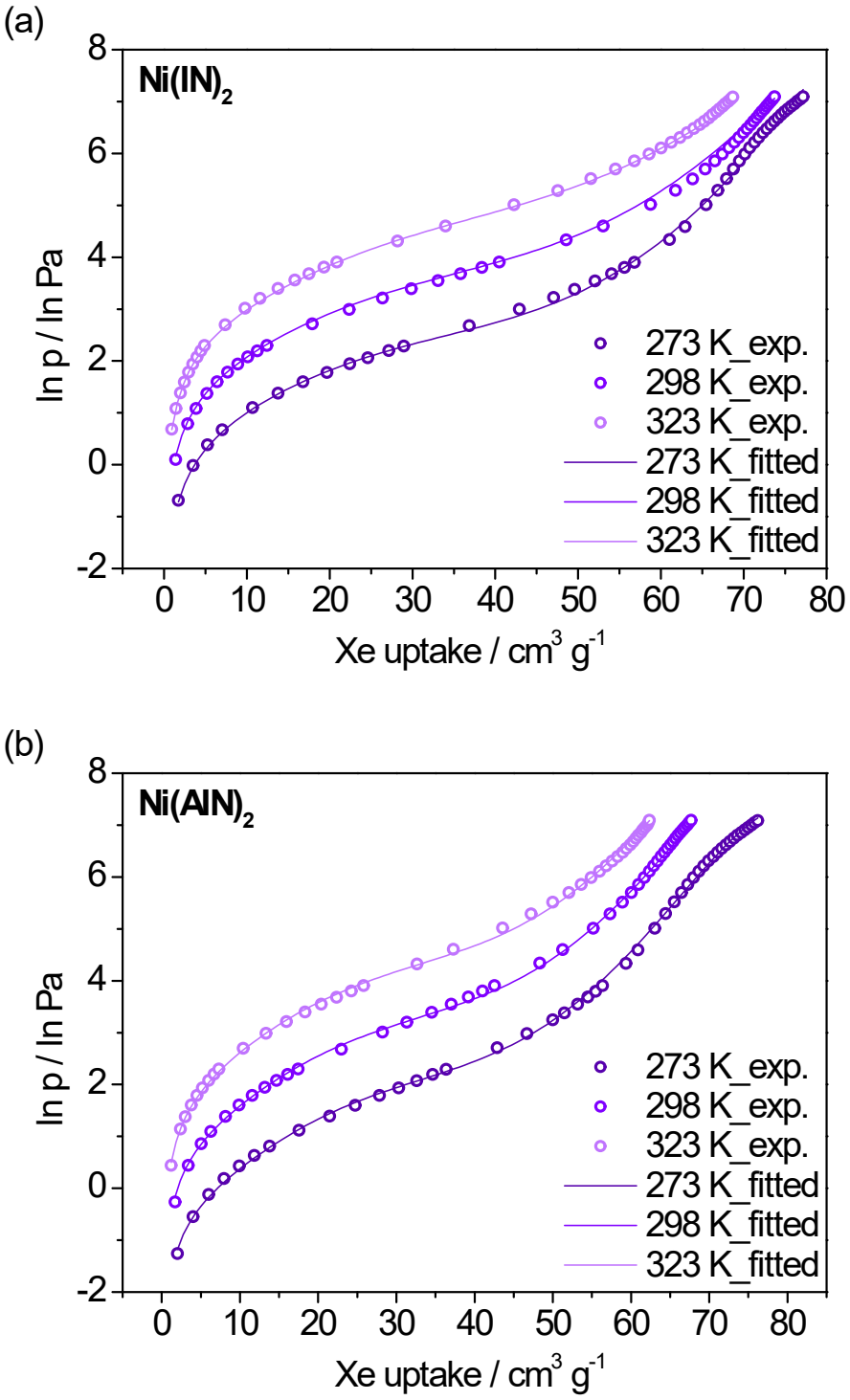

Fig. S19 Fit of Xe isotherms of (a) **Ni(IN)$_2$** and **Ni(AIN)$_2$** to Virial model at 273, 298, and 323 K.

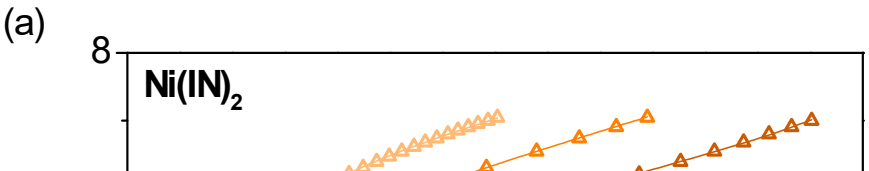

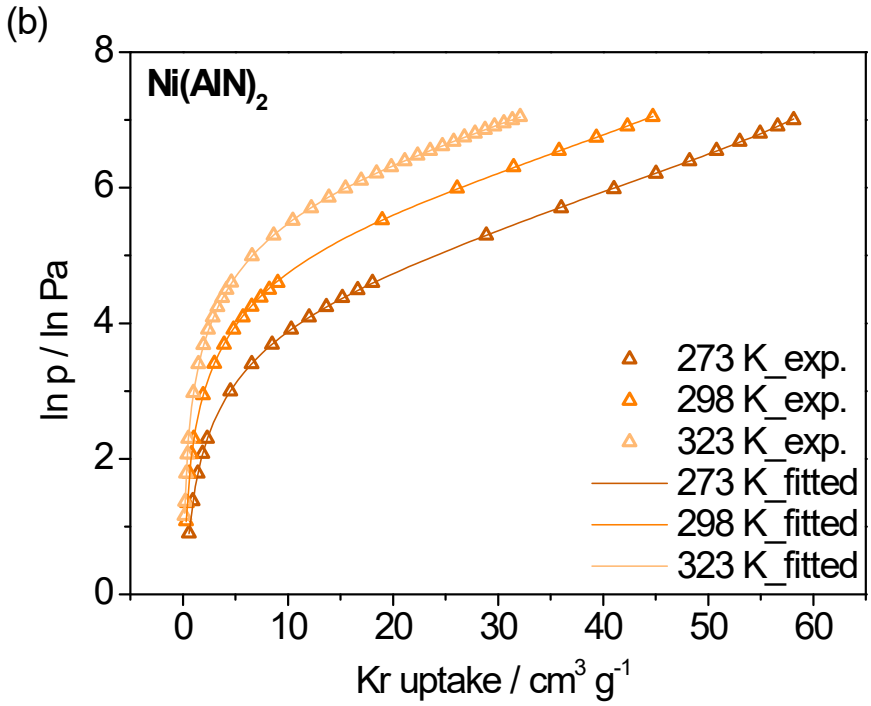

Fig. S20 Fit of Kr isotherms of (a) **Ni(IN)$_2$** and **Ni(AIN)$_2$** to Virial model at 273, 298, and 323 K.

Table S7 Summary of the fitted Virial parameters.

	$Ni(IN)_2$		**$Ni(AIN)_2$**	
	Xe	Kr	Xe	Kr
R^2	0.99871	0.99987	0.99941	0.99994
a_0	-3515.96193	-2409.54616	-3718.2789	-2691.17254
a_1	4.86037	-39.05158	-46.1776	-20.10889
a_2	-0.09511	1.48216	3.15982	0.80286
a_3	-0.02449	-0.00644	-0.09845	6.78315×10^{-4}
a_4	6.16344×10^{-4}	-3.03783×10^{-4}	0.00143	-3.07851×10^{-4}
a_5	-2.94814×10^{-6}	2.12851×10^{-6}	-7.66573×10^{-6}	2.10276×10^{-6}
b_0	11.66101	10.61068	11.86847	11.26186
b_1	-0.05411	0.15388	0.09114	0.09719
b_2	0.00439	-0.00623	-0.00276	-0.00412
b_3	-5.76393×10^{-5}	7.77839×10^{-5}	3.198×10^{-5}	5.81577×10^{-5}

Table S8 Comparison of Xe uptake, Q_{st}, IAST selectivity, and Henry's selectivity of **Ni(IN)$_2$** and **Ni(AIN)$_2$** with other Xe-selective materials at 298 K.

MOF	Xe Uptake (cm^3 g^{-1})		$Q_{st, Xe}$ (kJ mol^{-1})	IAST Selectivity (2:8, Xe/Kr)	Henry's Selectivity	ref.
	0.2 bar	1 bar				
ZJU-74a-Pd	58.82	63.00	45.5	103.4		6
CopzNi	58.69	73.92	38.5	14		7
MOF-Cu-H	58.27	71.65	33.34	16.7	15.8	8
Ni_2(m-dobdc)	58.12	124.79	28.3	10.1		9
Co_2(m-dobdc)	58.12	134.19	27.3	11.8		9
ECUT-60	51.07	96.32	30	11.4	11.6	10
MOF-505	49.49	49.49			6.8	11
Ag@MOF-74-Ni	46.22	108.40		6.8		12
ZLU-C2	46.14	57.57	28	19.1	19	13
$Zn(ox)_{0.5}$(trz)	45.91	61.01	29	10.2	12.5	14
Al-CDC	42.33	54.88	34.9	10.7	9.86	15
SIFSIX-3-Zn	41.51	69.18	30	9.2		16
NU-200	41.22	110.00	38	9.3		17
Ag-MOF-303	40.97	75.00	28.2	10.4		18
Al-Fum-Me	39.65	67.42		10	12.5	19
Ca-SINAP-1	37.15	64.46	29.2	10.04	10.32	20
SBMOF-2	32.77	63.87	26.4	10	8.6	21
Cu-MOF-303	32.28	71.65	24.4	8.2		18
MIL-120	31.85	44.59	31.5	9.6		22
NKMOF-1-Ni	30.29	48.57	34.2	5.2		23
$Co_3(HCOO)_6$	30.22	43.96	28	12 [a]	8.7	24
CaSDB (SBMOF-1)	28.39	32.90	37		20.5	25
CROFOUR-1-Ni	24.79	40.17	37.4	22	24.3	26
NU-403-PSDH	24.65	50.70	26	6.36		27
$Ni(4\text{-}DPDS)_2WO_4$	22.18	24.86	34.5	30.2		28
ECUT-50a	21.39	50.62	32	8		29
UTSA-74	20.90	60.45	24.4	8.4	7.85	30
ZIF-69	20.77	54.62	24.9		8.35	31
SCU-11	20.59	70.59			5.7	32
Co^{2+}-CPM-6	23.73	67.80	25.9	9.3		33
Zr-Fum-Me	23.12	42.77	30.9	11.7	14.8	34

SIFSIX-3-Cu	22.36	47.20		4.81 [b]		35
Y-csq-MOF-1	19.54	44.83	33.8	10.7 [a]	12.9	36
FJU-55	19.38	31.58	39.4	10		37
NU-1106	18.42	38.16			10	38
UiO-66	15.87	44.44	24.6	5.9	6.9	34
$Co_3C_8H_2O_{10}$	12.73	30.00	43.6	69.7	51.4	39
UiO-66-$NH_2(OMe)_2$	9.22	22.4			14.4	40
$Sr_4(TCPE)_2$	8.33	18.94	19.4	7		41
MOF-5	6.78	49.15	11.1	2.4		42
ZU-62	4.32	84.57				43
IISERP-MOF2	63.98	71.68		18.51	19.16	44
$Ni(IN)_2$	61.76	72.76	29.22	17.70	19.95	*This Work*
$Ni(AIN)_2$	57.33	66.61	30.95	20.32	23.19	

*a: at a ratio of 1:9 (v/v); b: calculated from the breakthrough results.

S4. Computational methods

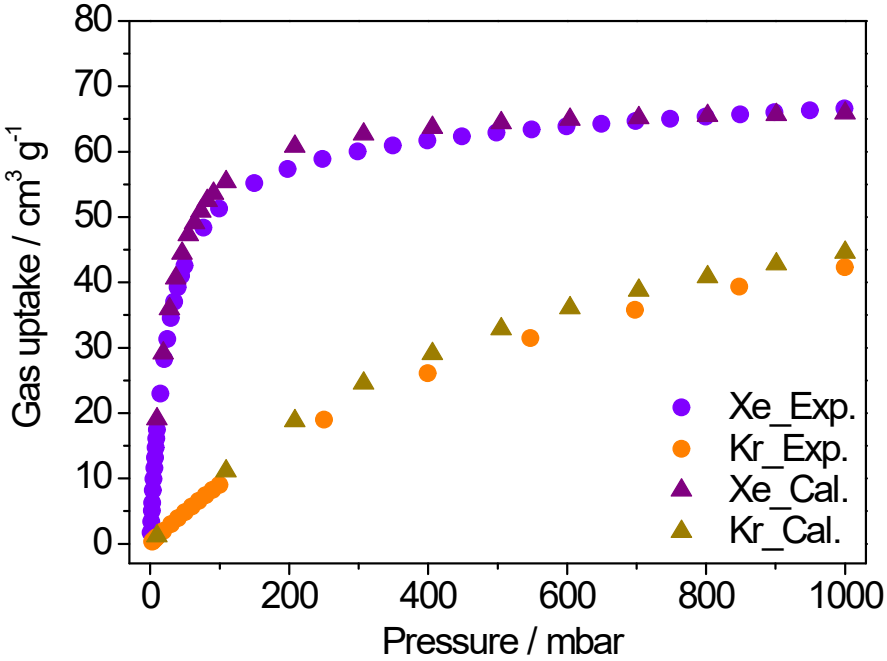

Fig. S21 Calculated and experimental isotherms of **Ni(AIN)$_2$** at 298 K.

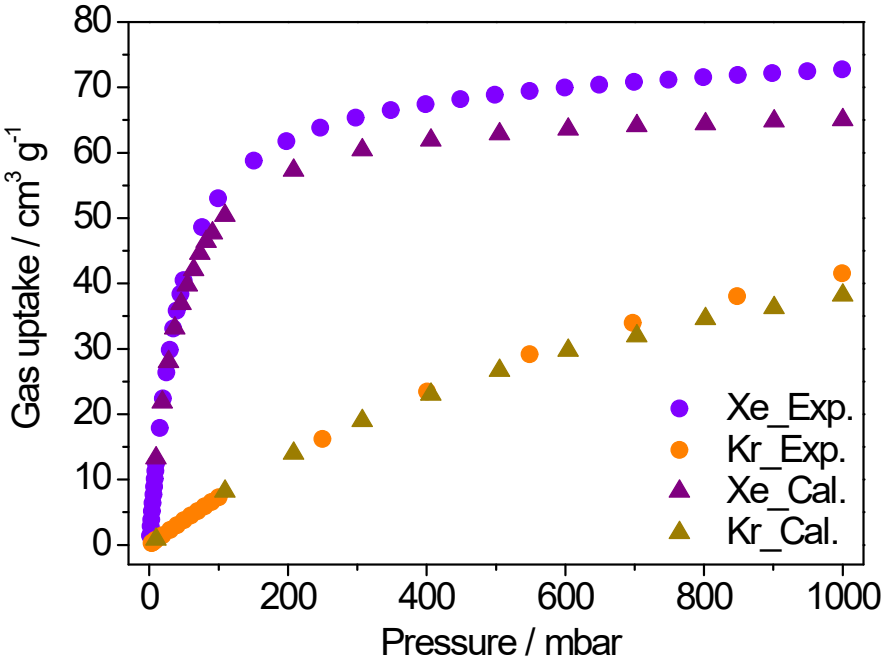

Fig. S22 Calculated and experimental isotherms of **Ni(IN)$_2$** at 298 K.

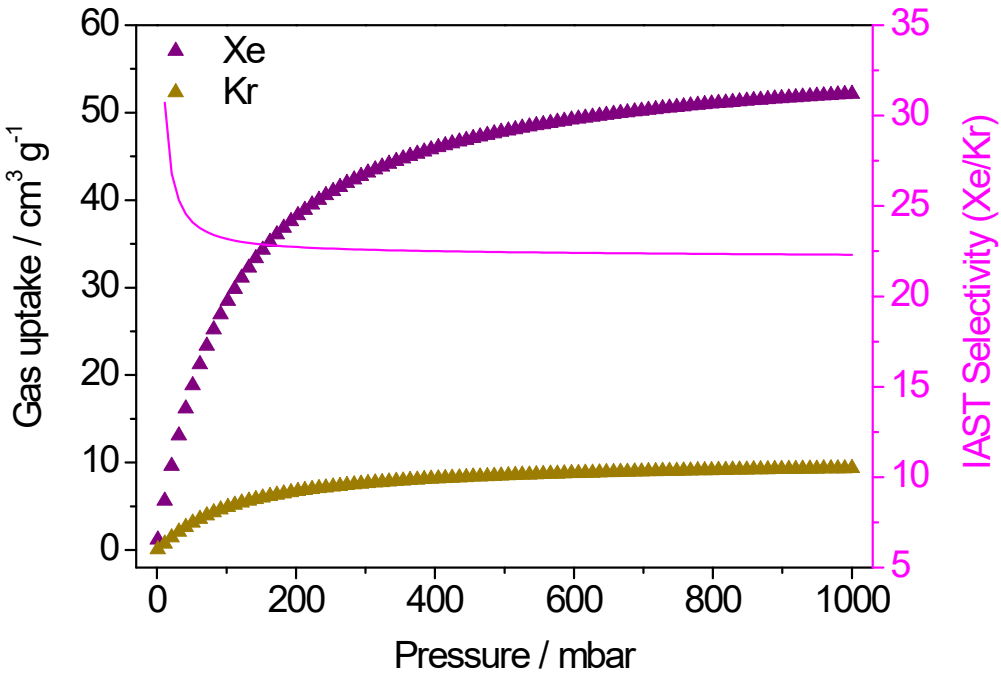

Fig. S23 IAST model-predicted adsorption isotherms and selectivity based on simulated isotherms of **Ni(AIN)$_2$**.

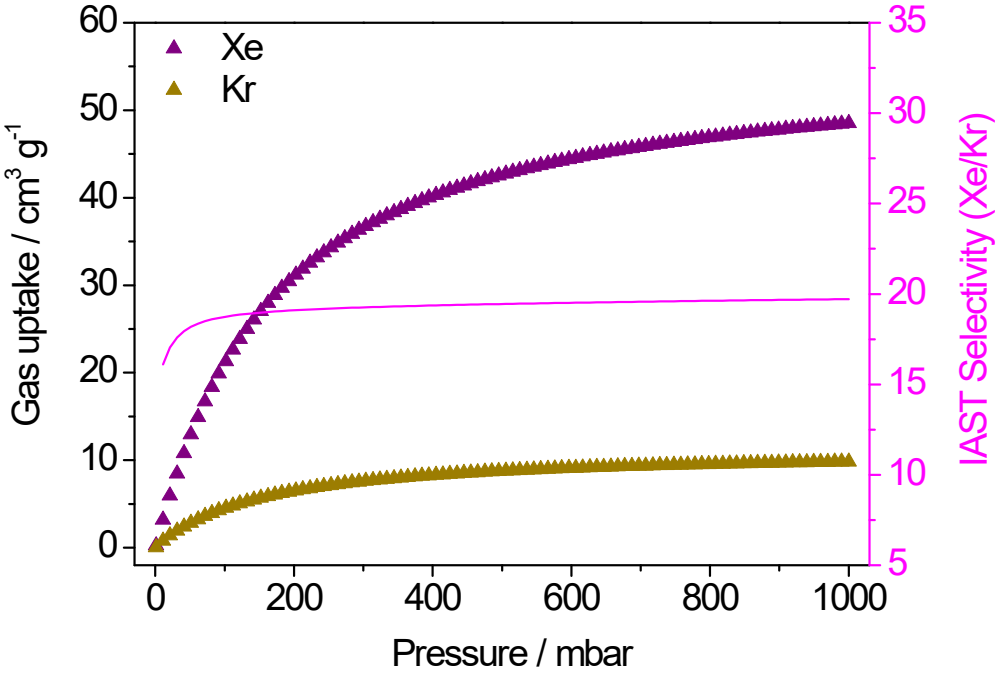

Fig. S24 IAST model-predicted adsorption isotherms and selectivity based on simulated isotherms of **Ni(IN)$_2$**.

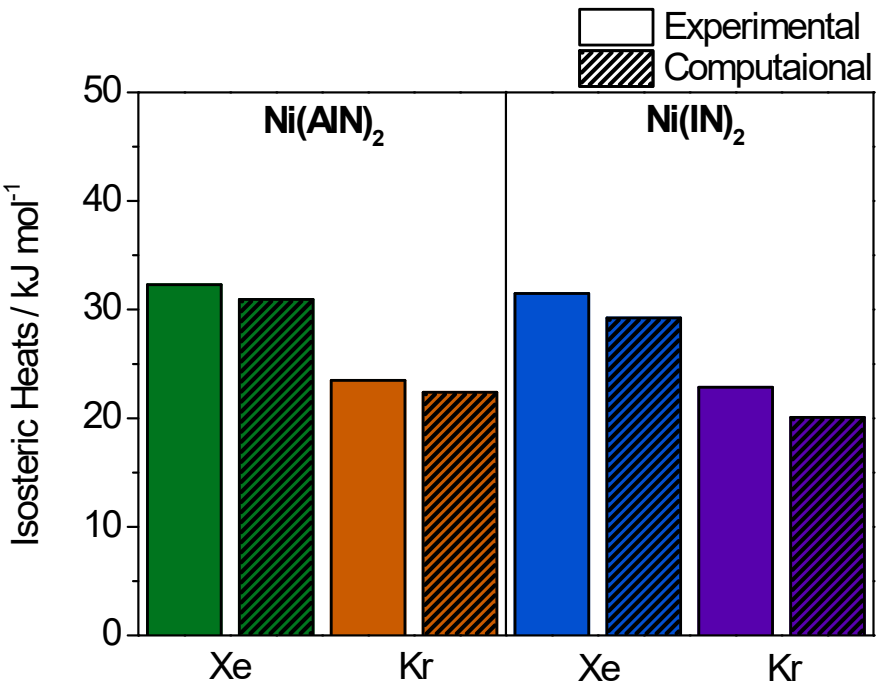

Fig. S25 Comparision of experimental and computational isosteric heats of Xe and Kr for each MOF.

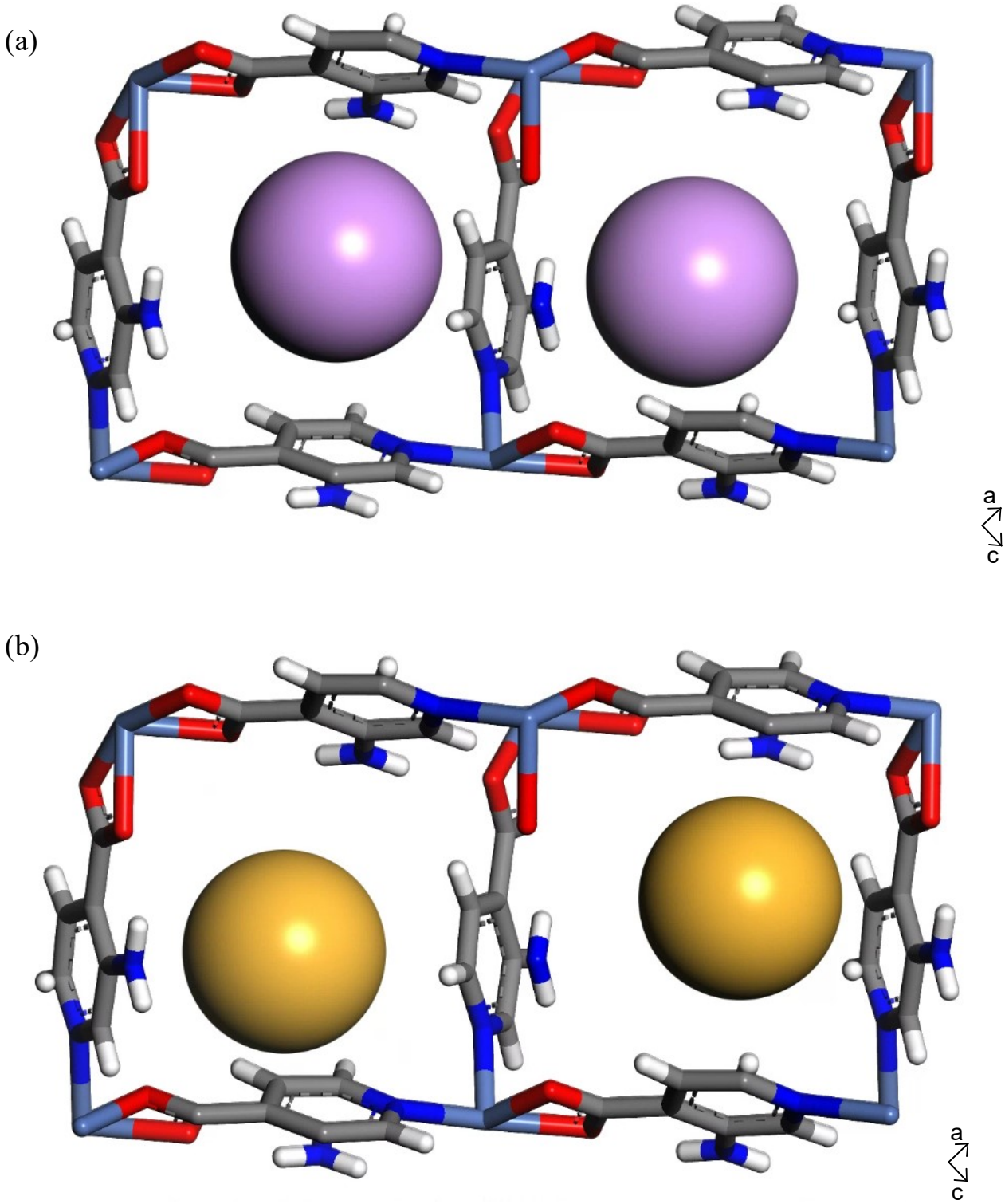

Fig. S26 Preferential Xe (a) and Kr (b) adsorption sites in **Ni(AIN)$_2$** along the b-axis direction, calculated by GCMC simulation. Color codes: Co, sky blue; C, gray; H, white; O, red; and N, blue, respectively.

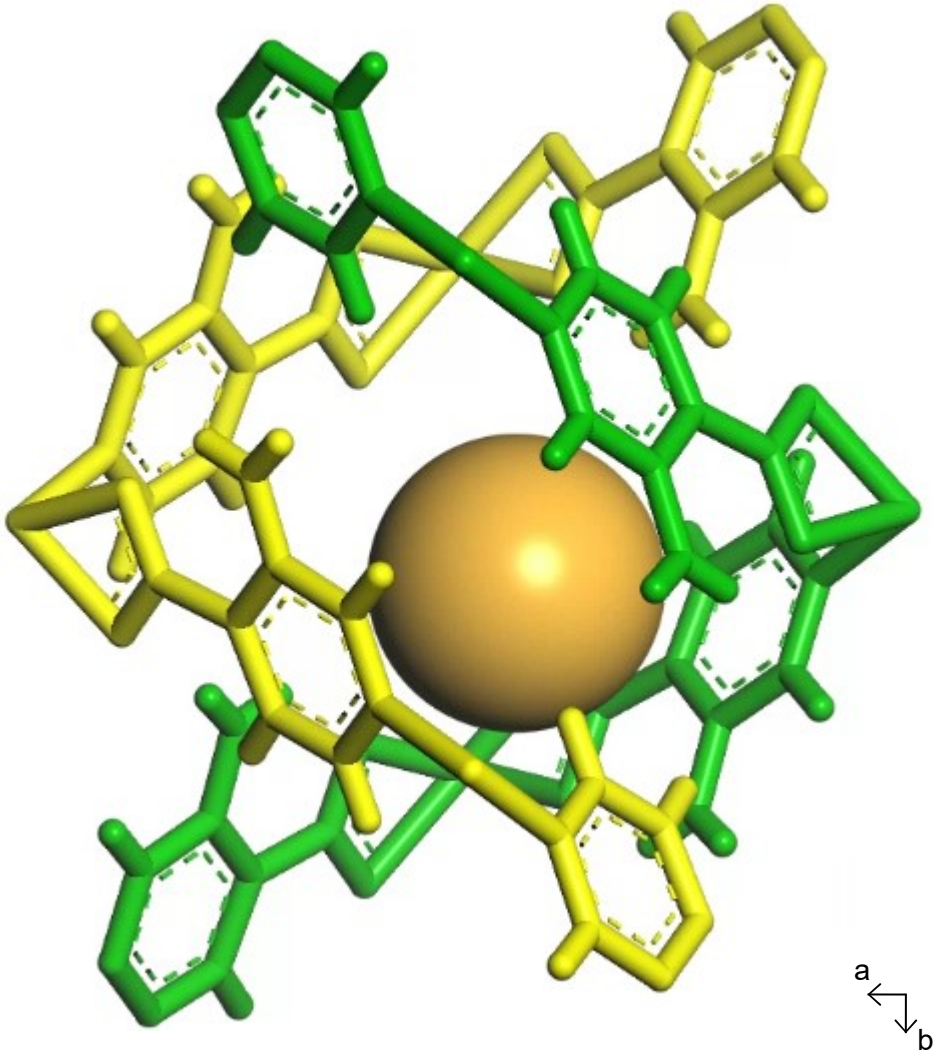

Fig. S27 Preferential Kr adsorption site in **Ni(AIN)$_2$** along the c-axis direction, calculated by GCMC simulation. The yellow and green fragments are interpenetrated.

(a)

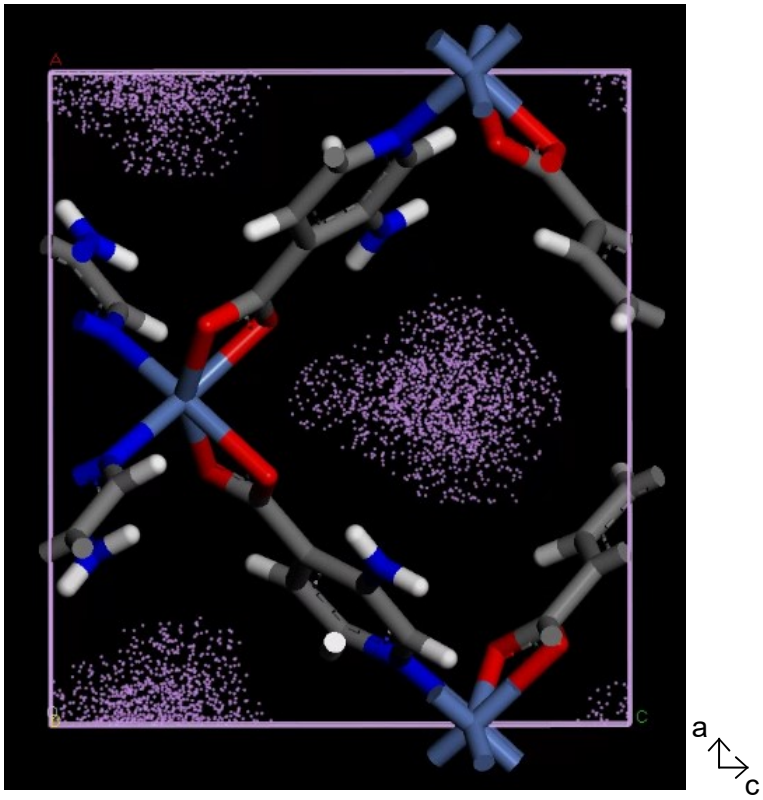

(b)

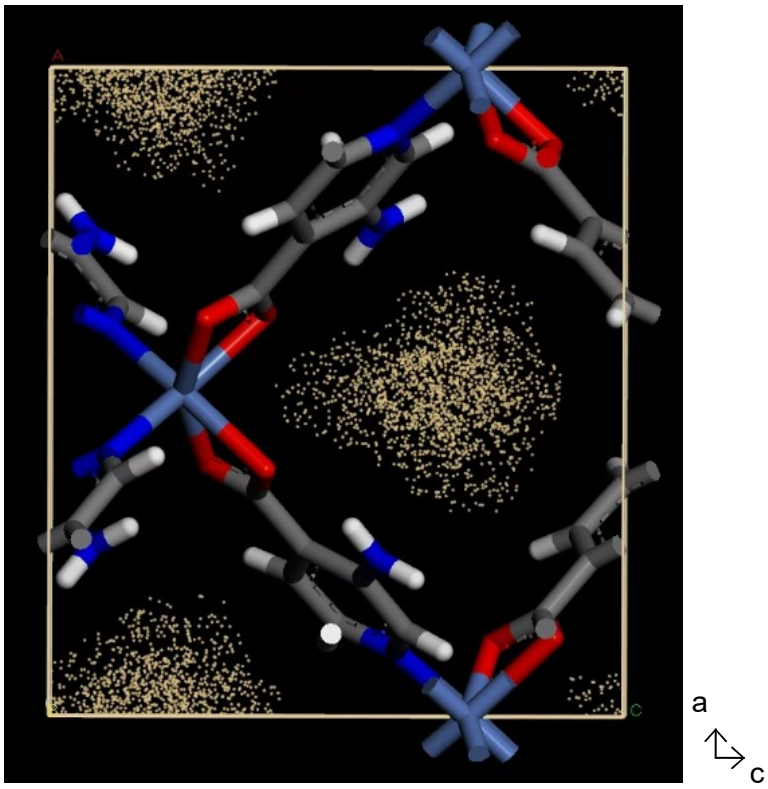

Fig. S28 Density distribution of Xe (a) and Kr (b) in the square pores of **Ni(AIN)$_2$**.

(a)

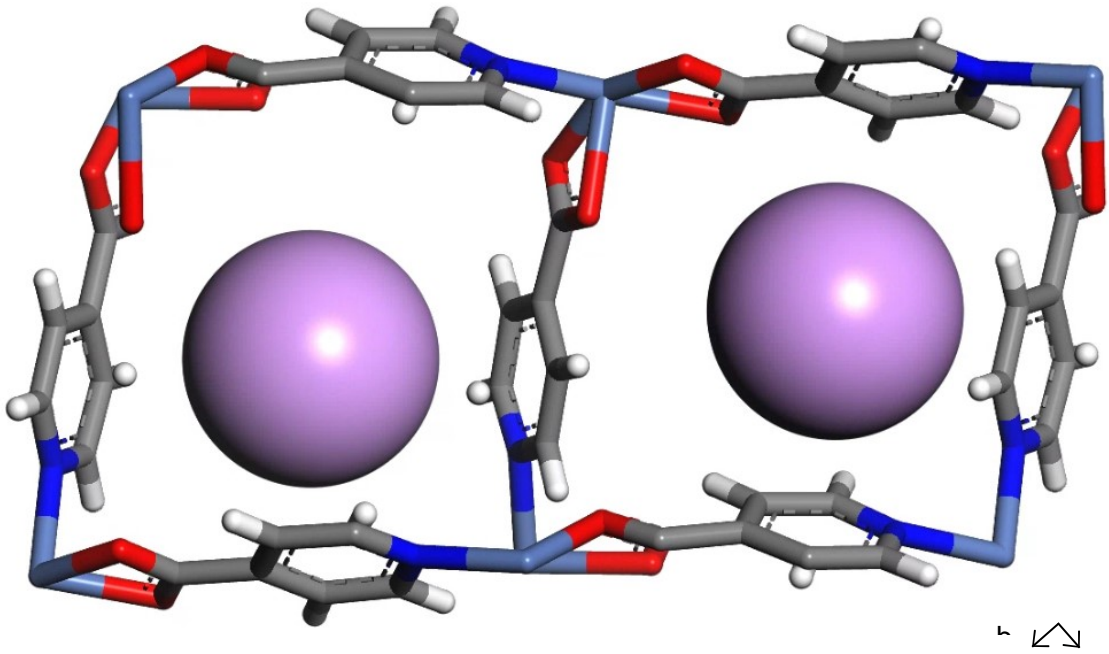

(b)

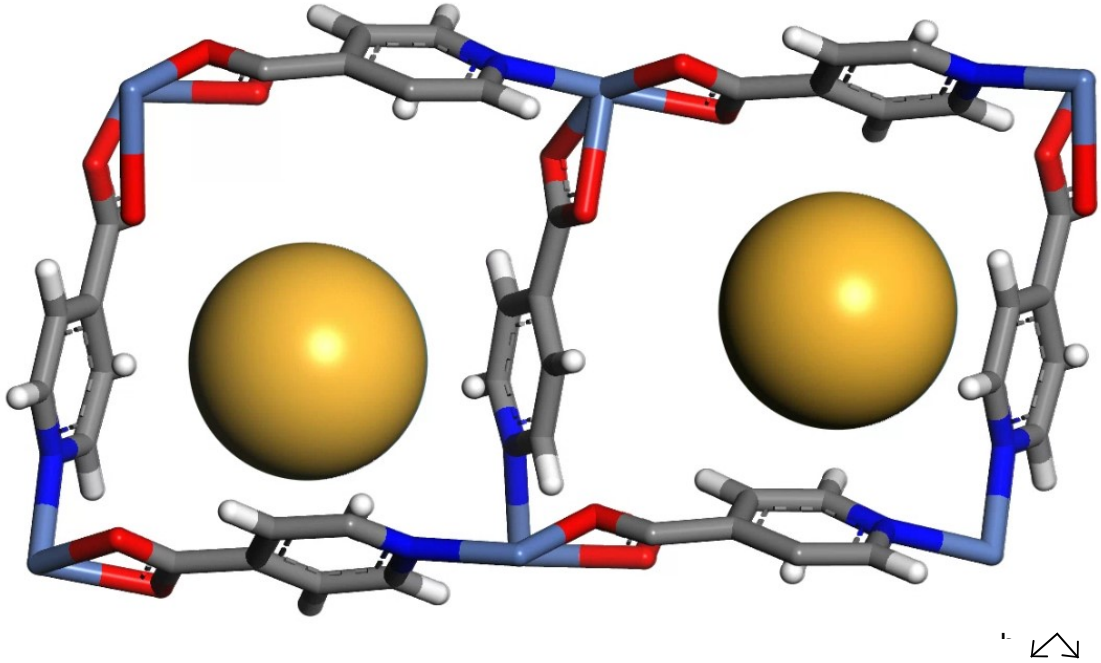

Fig. S29 Preferential Xe (a) and Kr (b) adsorption sites in **Ni(IN)$_2$** along the b-axis direction, calculated by GCMC simulation. Color codes: Co, sky blue; C, gray; H, white; O, red; and N, blue, respectively.

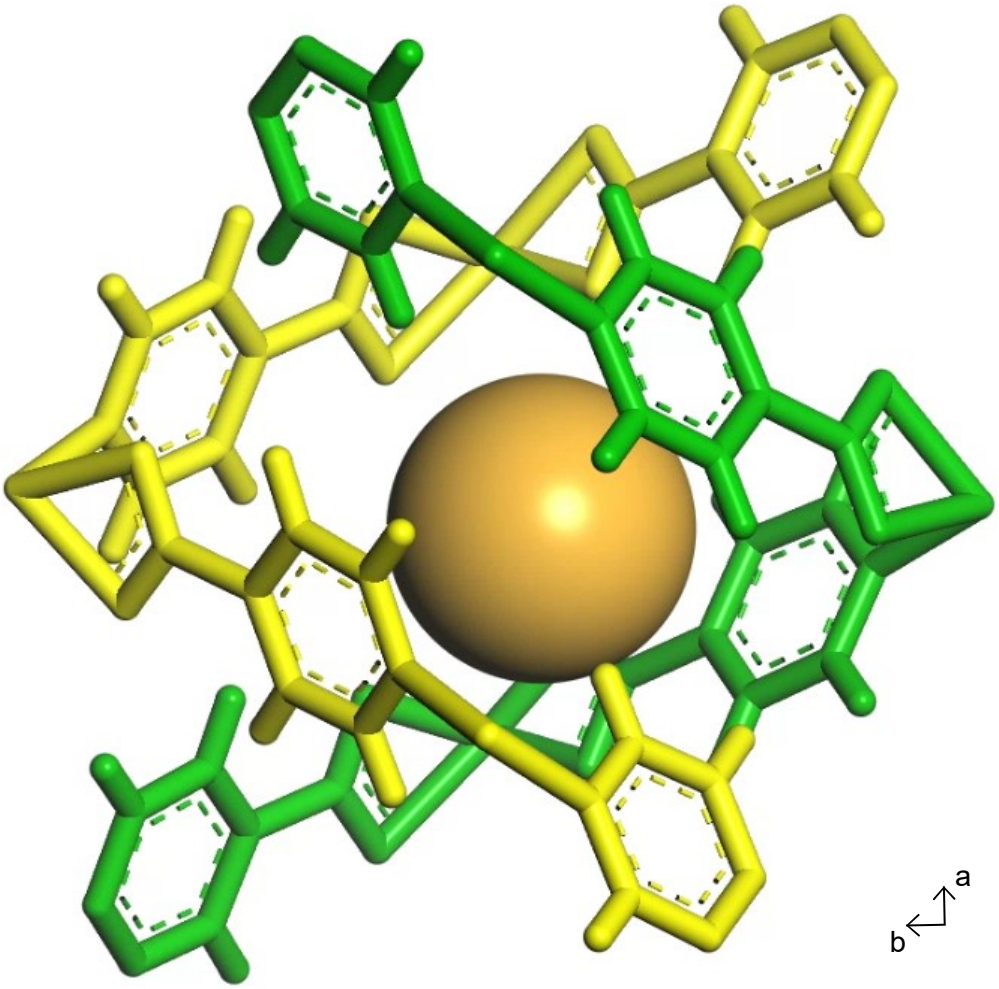

Fig. S30 Preferential Kr adsorption site in **Ni(IN)$_2$** along the c-axis direction, calculated by GCMC simulation. The yellow and green fragments are interpenetrated.

(a)

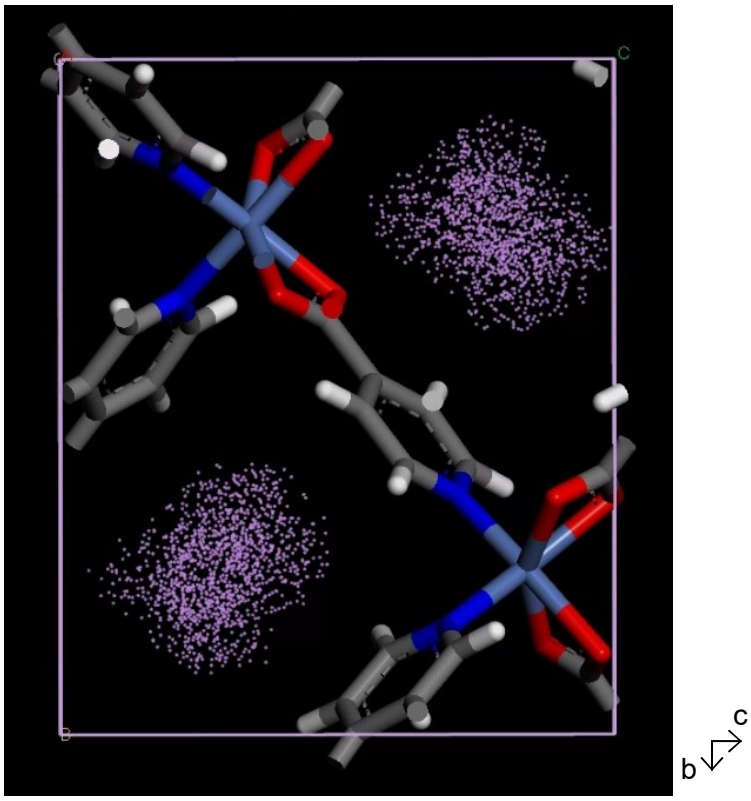

(b)

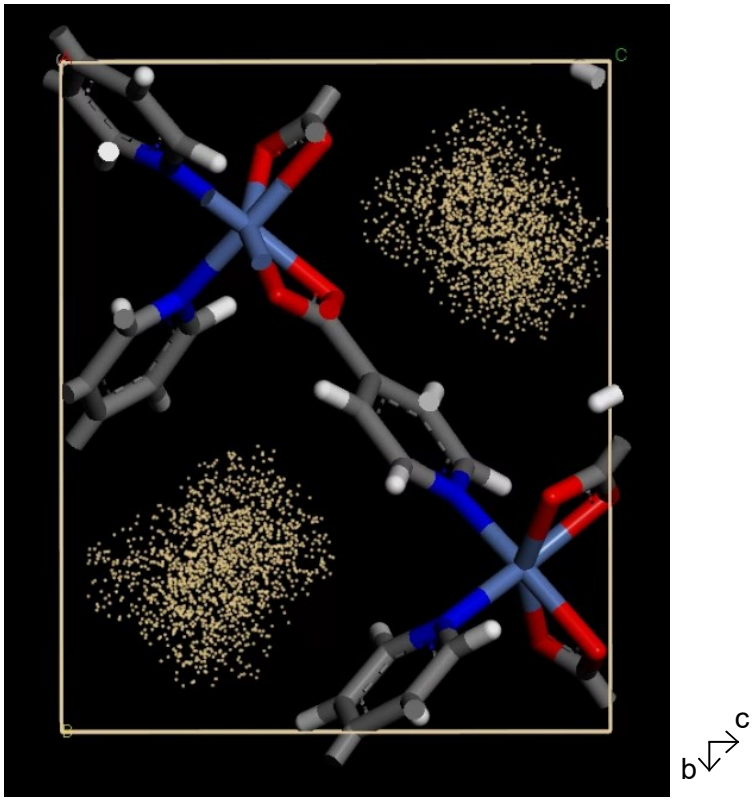

Fig. S31 Density distribution of Xe (a) and Kr (b) in the square pores of **Ni(IN)$_2$**.

S5. Breakthrough experiments

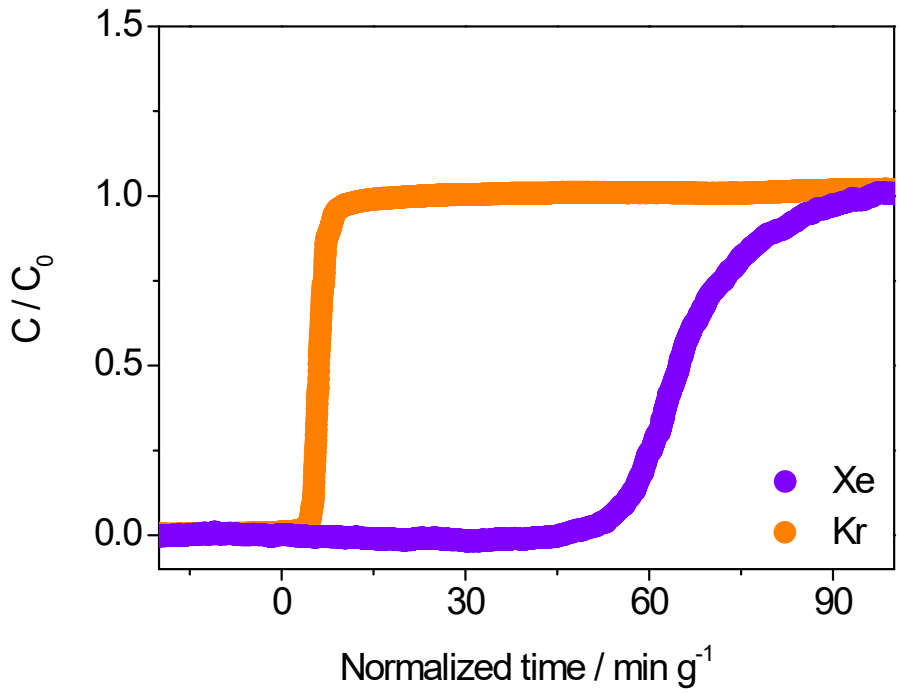

Fig. S32 Breakthrough curves of **Ni(AIN)$_2$** in a mixture of Xe/Kr with a volumetric ratio of 2:8 (Xe:Kr, v/v) at 298 K and 1 bar.

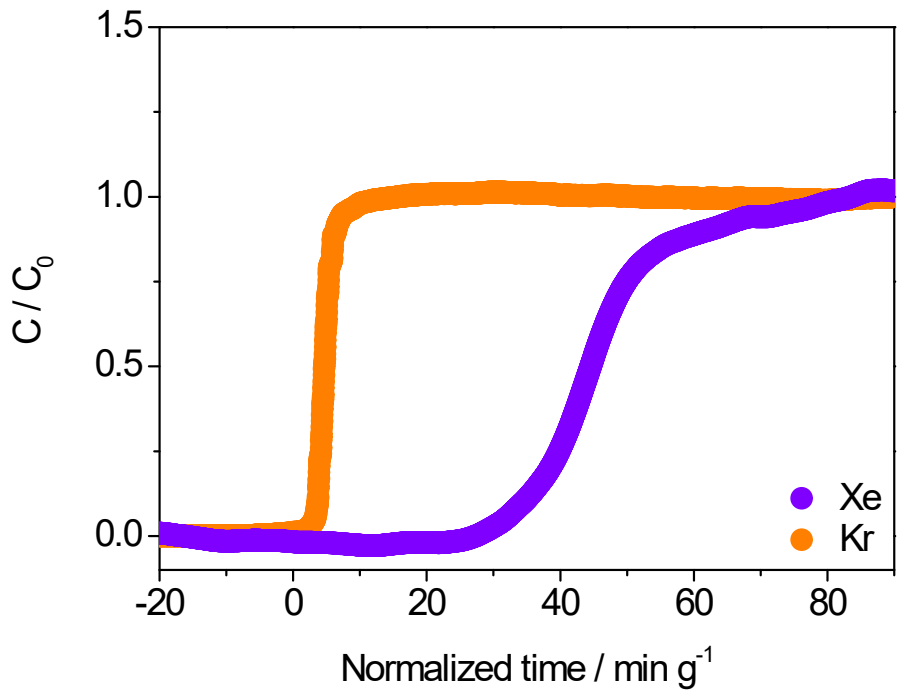

Fig. S33 Breakthrough curves of **Ni(IN)$_2$** in a mixture of Xe/Kr with a volumetric ratio of 2:8 (Xe:Kr, v/v) at 298 K and 1 bar.

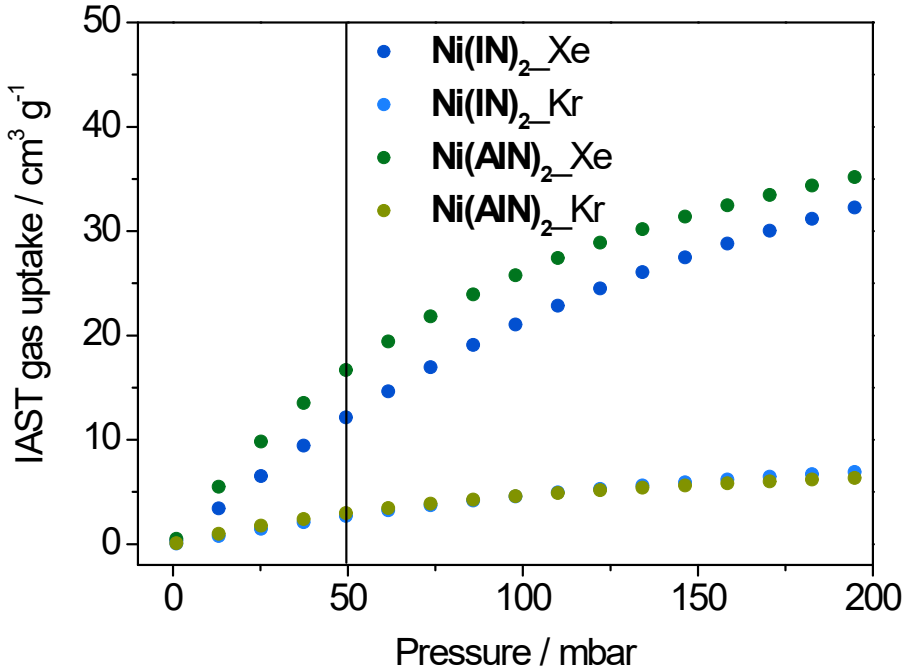

Fig. S34 IAST-predicted isotherms in a mixture of Xe/Kr with a volumetric ratio of 2:8 (Xe:Kr, v/v) at 298 K. The solid line represents a pressure of 50 mbar.

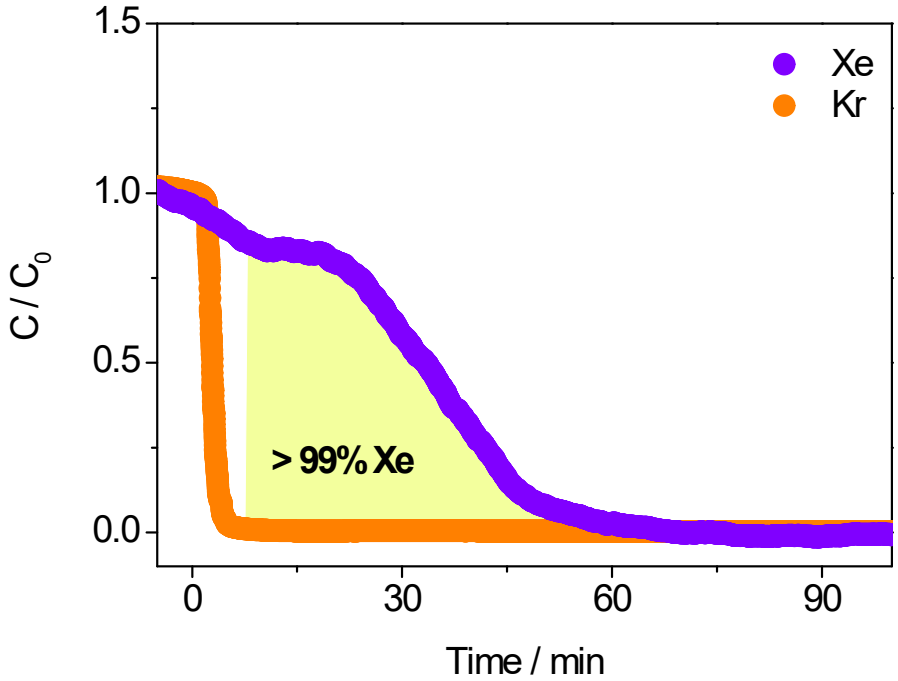

Fig. S35 Desorption curves of **Ni(AIN)$_2$** after the breakthrough curve measurement.

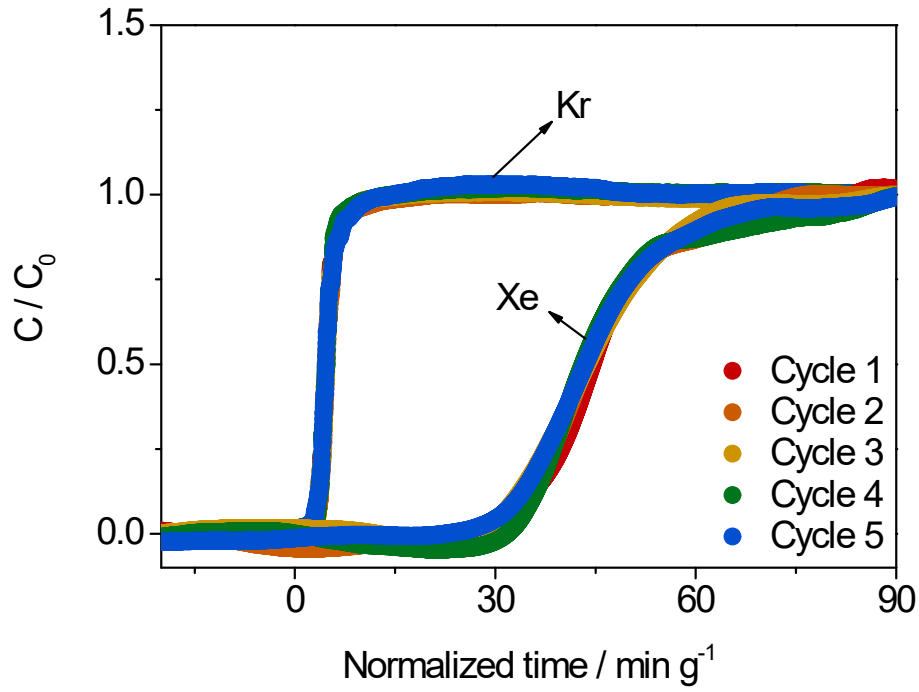

Fig. S36 Cycling breakthrough tests of **Ni(IN)$_2$** under dry conditions in a volumetric ratio of 2:8 (Xe:Kr, v/v) at 298 K and 1 bar.

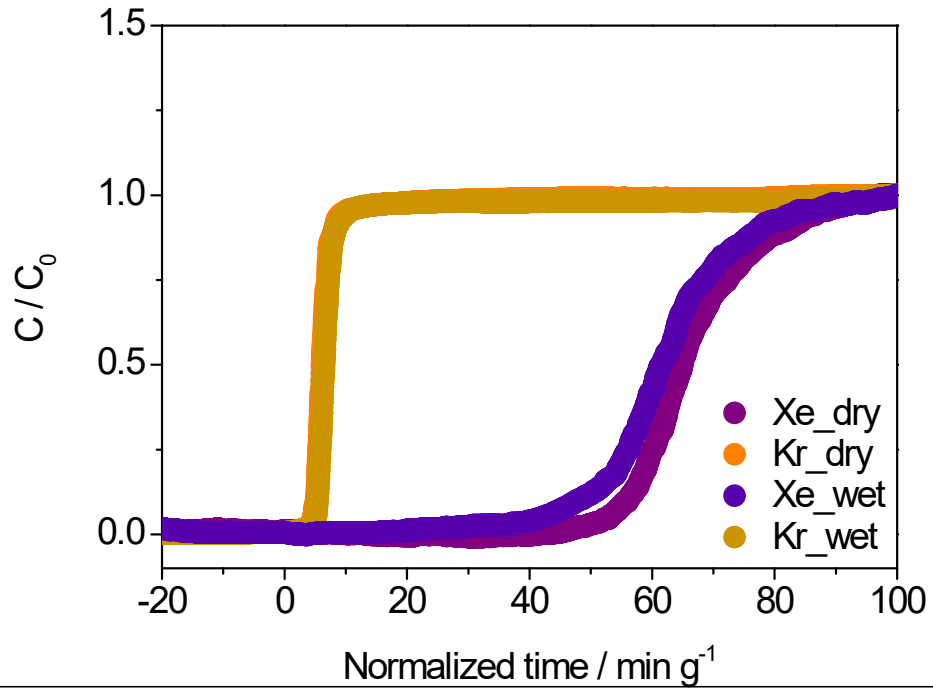

Fig. S37 Breakthrough curves of **Ni(AIN)$_2$** under dry and humid (40% RH) conditions.

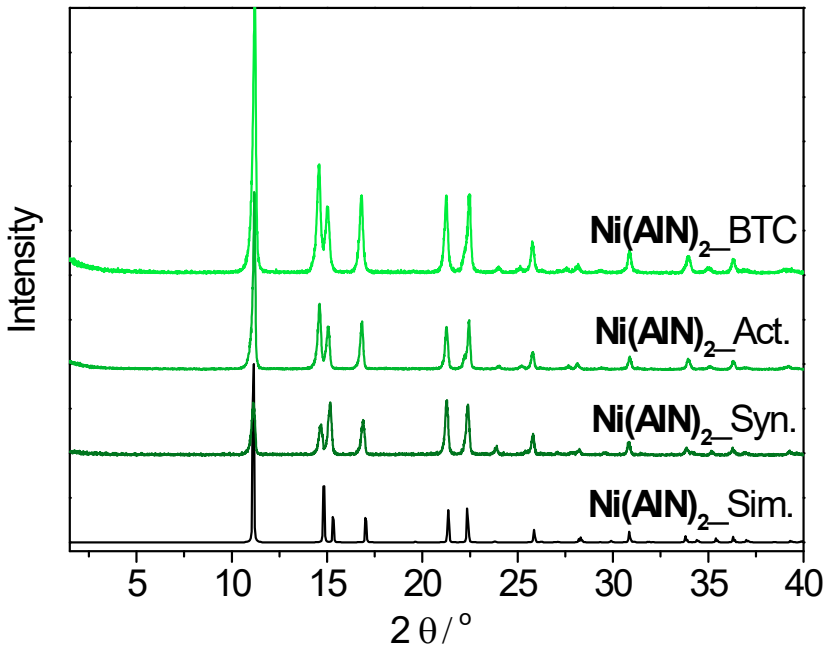

Fig. S38 PXRD profiles of simulated, synthesized, and activated **Ni(AIN)$_2$** after all breakthrough curve measurements.

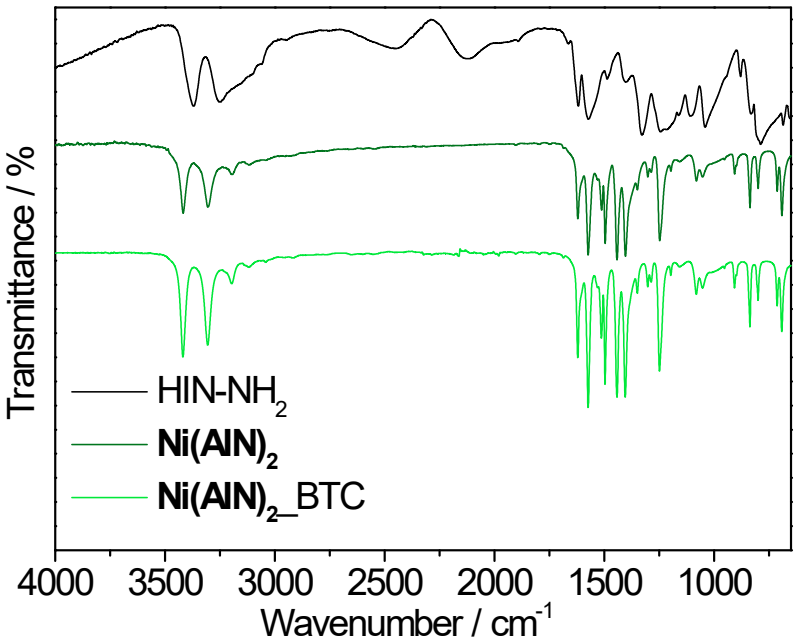

Fig. S39 IR spectra of pristine **Ni(AIN)$_2$** after all breakthrough curve measurements.

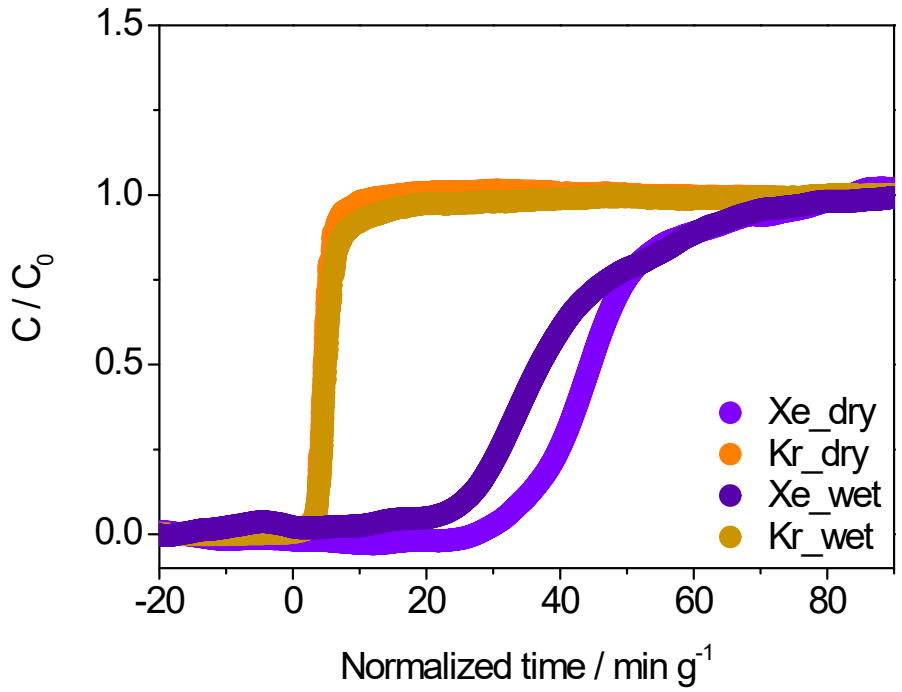

Fig. S40 Breakthrough curves of **Ni(IN)$_2$** under dry and humid (40% RH) conditions.

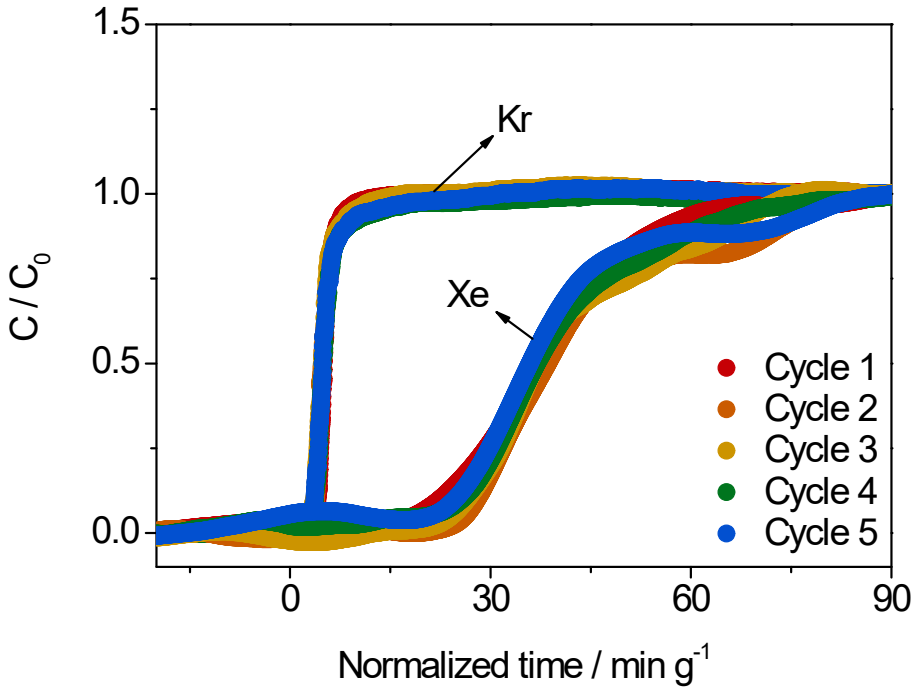

Fig. S41 Cycling breakthrough tests of **Ni(IN)$_2$** under 40% RH in a volumetric ratio of 2:8 (Xe:Kr, v/v) at 298 K and 1 bar.

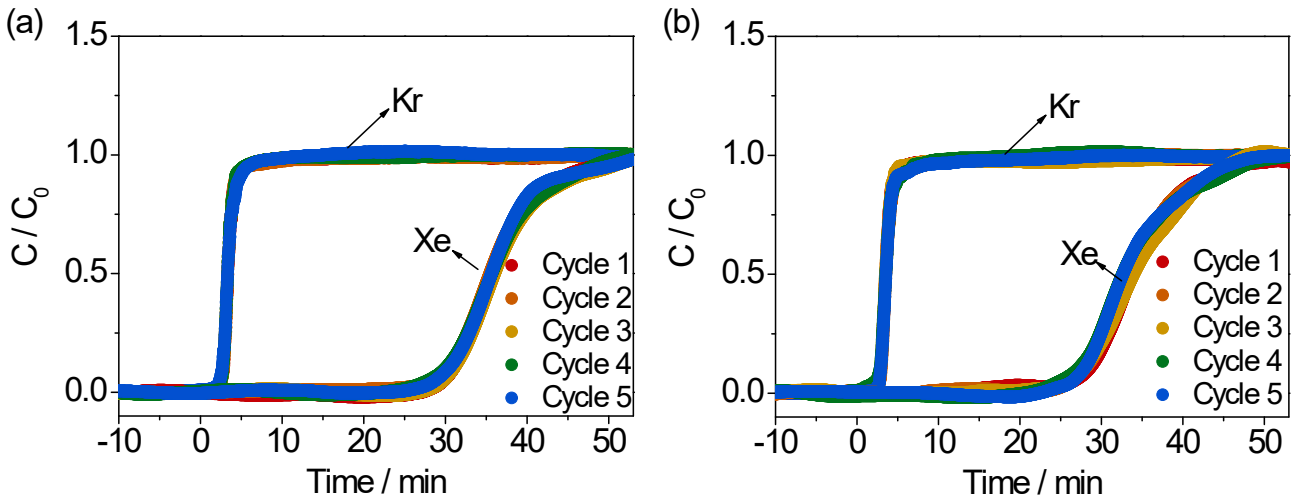

Fig. S42 Cycling breakthrough tests of **Ni(AIN)$_2$** under (a) dry and (b) 40% RH in a volumetric ratio of 2:8 (Xe:Kr, v/v) in original time at 298 K and 1 bar.

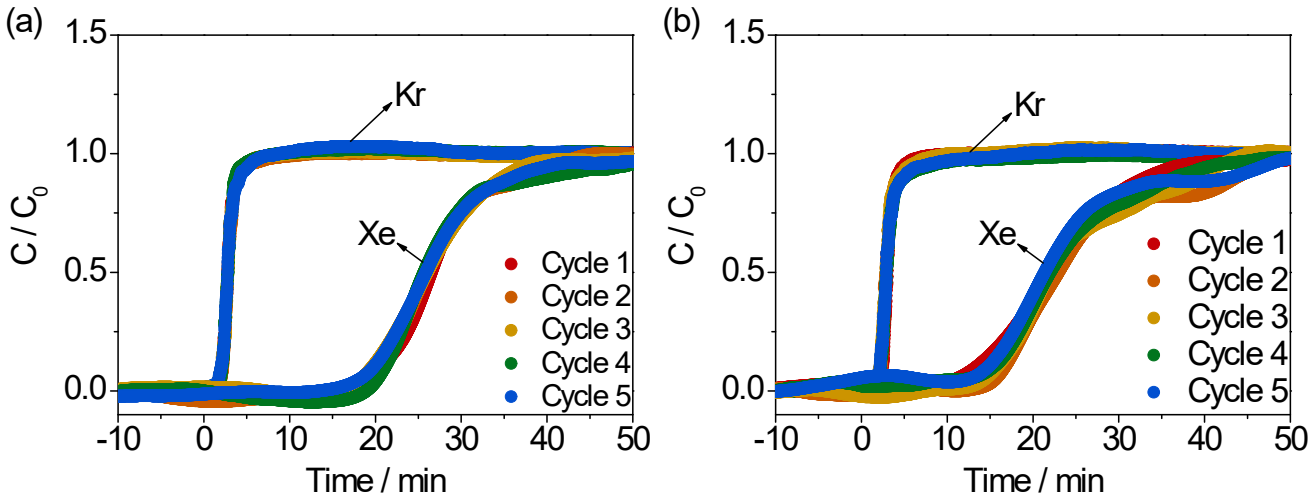

Fig. S43 Cycling breakthrough tests of **Ni(IN)$_2$** under (a) dry and (b) 40% RH in a volumetric ratio of 2:8 (Xe:Kr, v/v) in original time at 298 K and 1 bar.

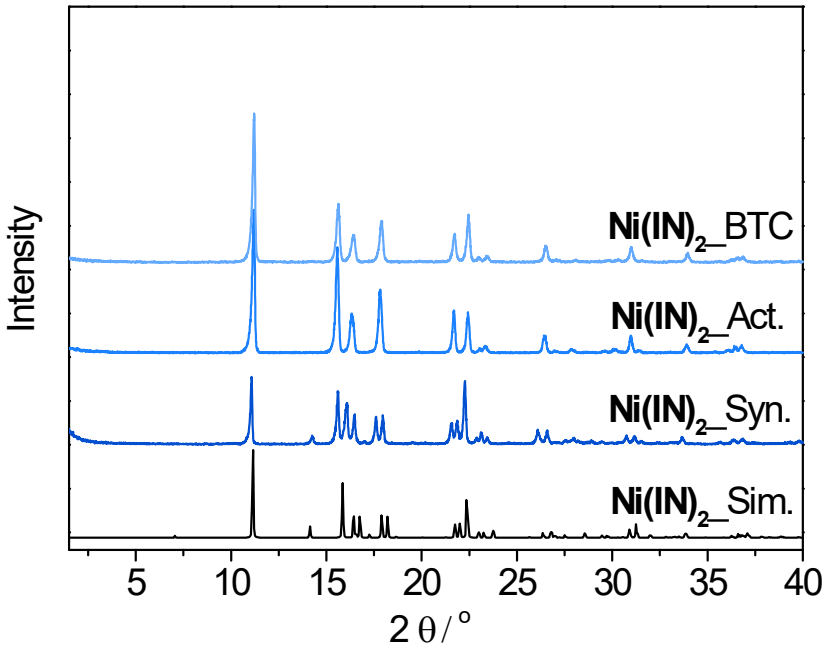

Fig. S44 PXRD profiles of simulated, synthesized, and activated **Ni(IN)$_2$** after all breakthrough curve measurements.

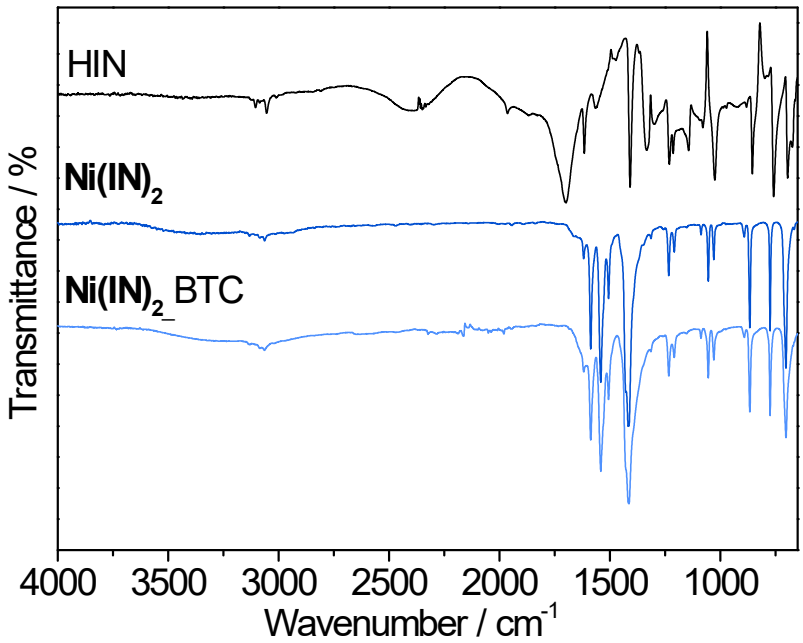

Fig. S45 IR spectra of **Ni(IN)$_2$** before and after all breakthrough curve measurements.

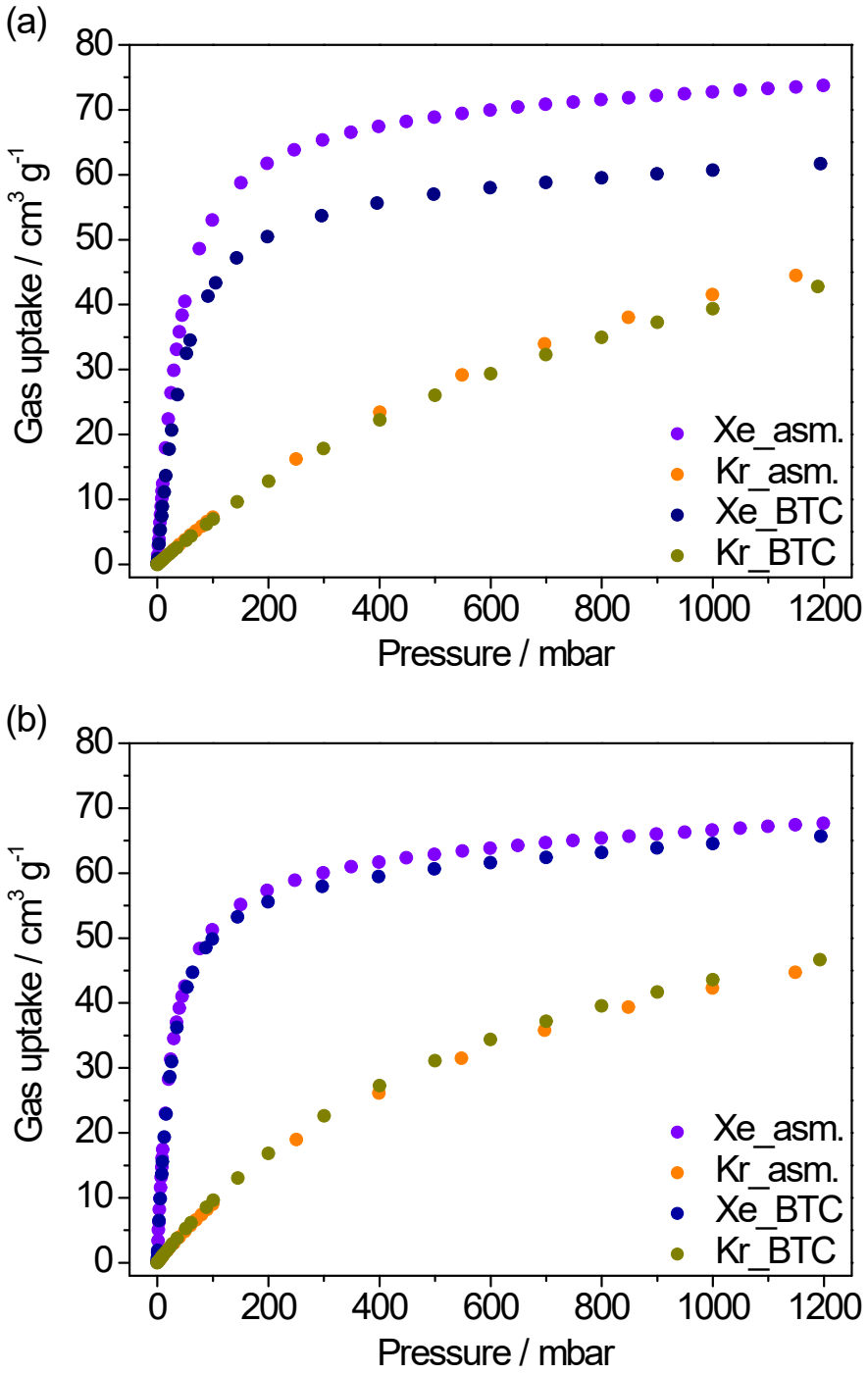

Fig. S46 Adsorption isotherms of (a) **Ni(IN)$_2$** and (b) **Ni(ANI)$_2$** before and after all breakthrough curve measurements.

S6. References

1. J. W. Shin, K. Eom and D. Moon, *J. Synchrotron Radiat.*, 2016, **23**, 369-373.
2. Z. Otwinowski and W. Minor, *Methods in Enzymology*, Academic Press, New York, 1997.
3. Z. Otwinowski, D. Borek, W. Majewski and W. Minor, *Acta Cryst.*, 2003, **A59**, 228-234.
4. *ChemMaster - Microtrac BEL Corp.*, Japan, 2019.
5. *Sorption Module - Accelrys Inc.*, San Diego, 2011.
6. J. Pei, X. W. Gu, C. C. Liang, B. Chen, B. Li and G. Qian, *J. Am. Chem. Soc.*, 2022, **144**, 3200-3209.
7. L. Guo, F. Zheng, Q. Xu, R. Chen, H. Sun, L. Chen, Z. Zhang, Q. Yang, Y. Yang, Q. Ren and Z. Bao, *Ind. Eng. Chem. Res.*, 2022, **61**, 7361-7369.
8. S. Xiong, Y. Gong, S. Hu, X. Wu, W. Li, Y. He, B. Chen and X. Wang, *J. Mater. Chem. A*, 2018, **6**, 4752-4758.
9. M. T. Kapelewski, J. Oktawiec, T. Runčevski, M. I. Gonzalez and J. R. Long, *Isr. J. Chem.*, 2018, **58**, 1138-1143.
10. H. Zhang, Y. Fan, R. Krishna, X. Feng, L. Wang and F. Luo, *Sci. Bull.*, 2021, **66**, 1073-1079.
11. Y.-S. Bae, B. G. Hauser, Y. J. Colón, J. T. Hupp, O. K. Farha and R. Q. Snurr, *Microporous Mesoporous Mater.*, 2013, **169**, 176-179.
12. J. Liu, D. M. Strachan and P. K. Thallapally, *Chem. Commun.*, 2014, **50**, 466-468.
13. J. Zhou, T. Ke, F. Steinke, N. Stock, Z. Zhang, Z. Bao, X. He, Q. Ren and Q. Yang, *J. Am. Chem. Soc.*, **144**, 14322-14329.
14. L. Yu, S. Xiong, Y. Lin, L. Li, J. Peng, W. Liu, X. Huang, H. Wang and J. Li, *Inorg. Chem.*, 2019, **58**, 15025-15028.
15. Z. Zhu, B. Li, X. Liu, P. Zhang, S. Chen, Q. Deng, Z. Zeng, J. Wang and S. Deng, *Sep. Purif. Technol.*, 2021, **274**, 119132.
16. Y. Liu, J. Liu and J. Hu, *BMC Chem. Eng.*, 2019, **1**, 3.
17. W. Gong, Y. Xie, T. D. Pham, S. Shetty, F. A. Son, K. B. Idrees, Z. Chen, H. Xie, Y. Liu, R. Q. Snurr, B. Chen, B. Alameddine, Y. Cui and O. K. Farha, *J. Am. Chem. Soc.*, 2022, **144**, 3737-3745.
18. H. Wang, Z. Shi, J. Yang, T. Sun, B. Rungtaweevoranit, H. Lyu, Y. B. Zhang and O. M. Yaghi, *Angew. Chem. Int. Ed.*, 2021, **60**, 3417-3421.
19. Z. Yan, Y. Gong, C.-T. Yang, X. Wu, B. Liu, Q. Liu, S. Xiong and S. Peng, *Cryst. Growth Des.*, 2020, **20**, 8039-8046.
20. X. L. Wu, Z. J. Li, H. Zhou, G. Yang, X. Y. Liu, N. Qian, W. Wang, Y. S. Zeng, Z. H. Qian, X. X. Chu and W. Liu, *Inorg. Chem.*, 2021, **60**, 1506-1512.
21. X. Chen, A. M. Plonka, D. Banerjee, R. Krishna, H. T. Schaef, S. Ghose, P. K. Thallapally and J. B. Parise, *J. Am. Chem. Soc.*, 2015, **137**, 7007-7010.
22. P. Zhang, Y. Zhong, Q. Yao, X. Liu, Y. Zhang, J. Wang, Q. Deng, Z. Zeng and S. Deng, *J. Chem. Eng. Data*, 2020, **65**, 4018-4023.
23. T. Wang, Y. L. Peng, E. Lin, Z. Niu, P. Li, S. Ma, P. Zhao, Y. Chen, P. Cheng and Z. Zhang, *Inorg. Chem.*, 2020, **59**, 4868-4873.
24. H. Wang, K. Yao, Z. Zhang, J. Jagiello, Q. Gong, Y. Han and J. Li, *Chem. Sci.*, 2014, **5**, 620-624.
25. G. Yu, Y. Liu, X. Zou, N. Zhao, H. Rong and G. Zhu, *J. Mater. Chem. A*, 2018, **6**, 11797-11803.
26. M. H. Mohamed, S. K. Elsaidi, T. Pham, K. A. Forrest, H. T. Schaef, A. Hogan, L. Wojtas, W. Xu, B. Space, M. J. Zaworotko and P. K. Thallapally, *Angew. Chem. Int. Ed.*, 2016, **55**, 8285-8289.
27. K. B. Idrees, Z. Chen, X. Zhang, M. R. Mian, R. J. Drout, T. Islamoglu and O. K. Farha, *Chem. Mater.*, 2020, **32**, 3776-3782.

28. F. Zheng, L. Guo, R. Chen, L. Chen, Z. Zhang, Q. Yang, Y. Yang, B. Su, Q. Ren and Z. Bao, *Angew. Chem. Int. Ed.*, 2022, **61**, e202116686.
29. L. Wang, W. Liu, J. Ding, H. Zhang, Y. Zhu and F. Luo, *Cryst. Growth Des.*, 2021, **21**, 954-959.
30. Y. Tao, Y. Fan, Z. Xu, X. Feng, R. Krishna and F. Luo, *Inorg. Chem.*, 2020, **59**, 11793-11800.
31. S. Luo, F. Ma, X. Wang, M. Yuan, L. Chen, S. Qiu, Q. Tang and S. Wang, *J. Radioanal. Nucl. Chem.*, 2020, **324**, 1275-1281.
32. Y. Wang, W. Liu, Z. Bai, T. Zheng, M. A. Silver, Y. Li, Y. Wang, X. Wang, J. Diwu, Z. Chai and S. Wang, *Angew. Chem. Int. Ed.*, 2018, **57**, 5783-5787.
33. B.-Y. Liu, Y.-J. Gong, X.-N. Wu, Q. Liu, W. Li, S.-S. Xiong, S. Hu and X.-L. Wang, *RSC Adv.*, 2017, **7**, 55012-55019.
34. Z. Yan, Y. Gong, B. Chen, X. Wu, Q. liu, L. Cui, S. Xiong and S. Peng, *Sep. Purif. Technol.*, 2020, **239**, 116514.
35. D. Banerjee, C. M. Simon, A. M. Plonka, R. K. Motkuri, J. Liu, X. Chen, B. Smit, J. B. Parise, M. Haranczyk and P. K. Thallapally, *Nat. Commun.*, 2016, **7**, 11831.
36. G. K. Angeli, C. Sartsidou, S. Vlachaki, I. Spanopoulos, C. Tsangarakis, A. Kourtellaris, E. Klontzas, G. E. Froudakis, A. Tasiopoulos and P. N. Trikalitis, *ACS Appl. Mater. Interfaces*, 2017, **9**, 44560-44566.
37. L. Gong, Y. Liu, J. Ren, A. M. Al-Enizi, A. Nafady, Y. Ye, Z. Bao and S. Ma, *Nano Res.*, 2022, **15**, 7559-7564.
38. R. R. Maldonado, X. Zhang, S. Hanna, X. Gong, N. C. Gianneschi, J. T. Hupp and O. K. Farha, *Dalton Trans.*, 2020, **49**, 6553-6556.
39. L. Li, L. Guo, Z. Zhang, Q. Yang, Y. Yang, Z. Bao, Q. Ren and J. Li, *J. Am. Chem. Soc.*, 2019, **141**, 9358-9364.
40. S.-J. Lee, S. Kim, E.-J. Kim, M. Kim and Y.-S. Bae, *Chem. Eng. J.*, 2018, **335**, 345-351.
41. J. Xiong, A. Li, Y. Fan, Z. Xu, H. Feng, Q. Gao, Q. Fan, Y. He, Z. Gao and F. Luo, *J. Solid State Chem.*, 2020, **288**, 121337.
42. J. A. Greathouse, T. L. Kinnibrugh and M. D. Allendorf, *Ind. Eng. Chem. Res.*, 2009, **48**, 3425-3431.
43. Q. Wang, T. Ke, L. Yang, Z. Zhang, X. Cui, Z. Bao, Q. Ren, Q. Yang and H. Xing, *Angew. Chem. Int. Ed.*, 2020, **59**, 3423-3428.
44. D. Chakraborty, S. Nandi, R. Maity, R. K. Motkuri, K. S. Han, S. Collins, P. Humble, J. C. Hayes, T. K. Woo, R. Vaidhyanathan and P. K. Thallapally, *Chem. Eng. J.*, 2020, **26**, 12544-12548.